MINERALOGY OF GAS HYDRATE BEARING SEDIMENT IN GREEN CANYON BLOCK 955 GULF OF MEXICO

Undergraduate Research Thesis
Submitted in partial fulfillment of the requirements for graduation
With research distinction in Earth Sciences
In the undergraduate colleges of
The Ohio State University

By

Ryan Heber
The Ohio State University
2017

Approved by

Ann Cook
School of Earth Sciences

TABLE OF CONTENTS

ABSTRACT

Mounting interest in natural gas hydrates as a possible future energy source has led to increasing research into their physical properties and formation. By defining the mineral assemblage of a silt dominated gas hydrate-bearing reservoir subsampled from cores recovered from Green Canyon block 955 in the Northern Gulf of Mexico on the UT-GOM2-01 expedition, a better model of hydrate reservoir properties can be constructed. Using x-ray computed tomography, x-ray diffraction, high resolution Leica microscope images, and the Rietveld method for a semi-quantitative refinement, mineral identification yielded a sediment primarily composed of quartz, with significant proportions of alkali feldspar and carbonate, and minor amounts of amphibole, micas, and clays. Due to limitations inherent to quantitative analysis, quartz, despite being the most abundant, was underestimated by the model, and albite, a feldspar mineral, was overestimated. Subsamples with the highest quartz content came from the section of the reservoir with the highest hydrate saturation. Subsamples with the highest clay content came form the section of the reservoir with the lowest hydrate saturation. Therefore, from a mineralogical perspective, the ideal natural gas hydrate reservoir is a course-grained sediment abundant in quartz and lacking in clays. Although drilling mud intrusion of high density barite and a smectite rich bentonite gel tainted the native mineralogy and accuracy of semi-quantitative measurement, performing further XRD tests will determine the foreign background and improve both qualitative and quantitative results.

ACKNOWLEDGEMENTS

I would like to thank Dr. Ann Cook for steadfastly advising my research, my lab partner Nikki Kinash, Dr. Julie Sheets, Dr. Derek Sawyer, Dr. Joel Johnson, and Dr. Anne Carey for contributing their insight and feedback, the Shell Exploration and Production Company, the SURE program, and the scholarship from William J Buschman Fund in Earth Sciences for providing the opportunity to conduct meaningful scientific research. I would also like to thank the The University of Texas at Austin, Dr. Peter Flemings and all of the UT-GOM2-01 scientists for collecting the cores. XRD scans and light optical images were acquired at the Subsurface Energy Materials Characterization and Analysis Laboratory (SEMCAL), School of Earth Sciences, The Ohio State University. This research was funded by the United States Department of Energy under award number DE-FE0023919.

LIST OF FIGURES

LIST OF TABLES

INTRODUCTION

Natural gas hydrates, with their rigid ice-like lattices, trap natural gas molecules in a water derived clathrate geometry under conditions of low temperature and moderate pressure (Sloan and Koh, 2007). The largest concentrations of gas hydrates occur in the sediment of marine continental margins and arctic permafrost. They are of interest as a future hydrocarbon source, accounting for 3×10^{18} grams of carbon in deep ocean settings (Buffett, 2004). In fully occupied methane clathrate, 1 cubic meter contains 164 cubic meters of methane gas (Kvenvolden, 1993). The ability to extract this resource with the efficiency of other hydrocarbon reservoirs could unlock a previously untapped economic resource. Therefore, understanding the formation and physical properties of gas hydrate reservoirs will continue to be on the forefront of hydrate research. Industrial success of will depend on the development of technology able to safely dissociate, store, and transfer gas hydrates (Arora et al., 2016)

Gas hydrates are also a potential contributor to global climate change (Ruppel and Kessler, 2016). Changes in temperature and pressure conditions, caused by warming oceans, disrupt the hydrate stability field, leading to destabilization, dissociation, and possibly, submarine landslides. The unbound gas molecules have the capacity to be released into the sediments they were once frozen in, possibly reaching the atmosphere and adding to the greenhouse feedback effect thus leading to more destabilization. Although, evidence of hydrate-derived methane gas reaching the atmosphere has yet to be found (Ruppel and Kessler, 2016.

Not only are the hydrates themselves of interest, but the reservoirs containing hydrate provide insight into the physical conditions needed for hydrate accumulation. In the Gulf of Mexico sediments are typically fall between sand and clay sized grains, with clay minerals like montmorillonite and muscovite (Armstrong-Altrin and Machain-Castillo, 2016). Sediments composed of Mississippi River inputs are high in quartz and illite (Devine, 1971). The geochemical characteristics of sediments may play a role in pore fluid chemistry, and therefore, gas hydrate formation, for example, surfactant micellar solutions (composed of unaggregated amphiphiles over the critical micellar concentration) increase gas hydrate formation rates by lowering the surface tension between water and hydrocarbons (Zhong and Rogers, 2000).

Other mechanisms for hydrate accumulation include biosurfactant producing microbes, which can increase gas solubility in water, thus decreasing the induction rate of gas hydrates (Roger and Lee, 2001), and submarine groundwater discharge which leads to free gas-water interaction in deep ocean sediments (Frederick and Buffett, 2016).

Gas hydrate accumulation is in part controlled by pressure and temperature. In marine settings, hydrates are stable in the uppermost tens to hundreds of meters of sediment overlaid by at least 330–615 meters of water (Milkov et al., 2000). Temperatures range from 0–15 degrees Celsius with the lower limit of stability being bounded by the geothermal gradient (Ruppel, 2007). Continental margins that fit in this narrow window, such as Green Canyon in the Northern Gulf of Mexico, are the targets for geoscientists interested in natural gas hydrates.

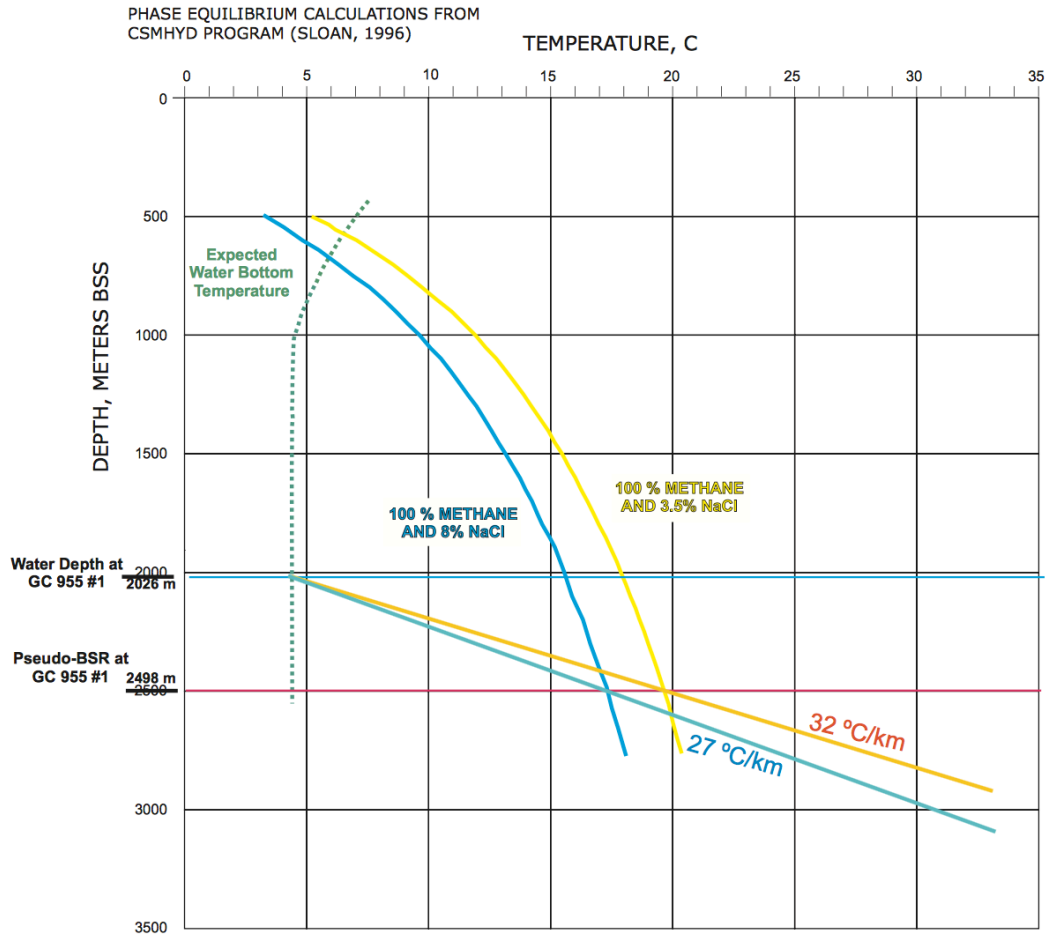

Figure 1: Gas hydrate phase stability for GC955 (McConnell et al., 2009).

Geologic Location and Background

Geology

Our area of interest is located in Green Canyon Block 955 (GC955), 330 km south of New Orleans in the northern Gulf of Mexico. The entire area is uplifted from a rising salt diaper. Salt movement has contributed to substantial deformation in the area, including uplift and faulting, creating pathways for fluid flow through the overlying fine grained sealing units up to the seafloor (Haines et al., 2015). Modeling of Green Canyon by Burwicz et al., (2017) revealed a potential gas hydrate volume of 3256 Mt, amounting to about 340 Mt of carbon. The base of the hydrate stability zone at Green Canyon Block 955 exists ~500 meters below the seafloor. Sediment within the stability zone rages from 5–20 degrees Celsius

The target reservoir is a buried Pleistocene submarine canyon levee system, ~ 400 m below seafloor, under 2 kilometers of water. The main coarse-grained reservoir at GC955 has high saturations of gas hydrate, ranging from 66-87%. The ~100 m reservoir has grains ranging from

20-200 μm (Flemings et al., 2017, in preparation), placing them in the course silt to fine sand classification, and a porosity of 40% based on logging while drilling data. (Collett et al., 2012)

In 2009, the Gas Hydrate Joint Industry Project (JIP) Leg 2 drilled three boreholes in GC955 (McConnell et al., 2009). The site selection was based on a variety of conditions such as pressure and temperatures within the hydrate stability zone, the presence of migrations pathways, and coarse grained sediment needed for high saturation. Moreover, geophysical anomalies of strong leading peaks (in zero-phase, North American polarity data) indicated the presence of gas hydrate. LWD data showed both high resistivity and high compressional velocity, pointing to reservoirs with high saturations of gas hydrate. Confirmation of gas hydrate occurred at two of the three holes (Hole GC955-H and Hole GC955-Q).

Core samples were not collected during JIP Leg 2, and so, in May 2017, the UT-GOM2-01 cruise set sail for GC955 to collect pressurized core from the coarse-grained gas hydrate reservoir. The first hole, H002, was drilled using a tool optimal for wireline logging purposes called a cutting shoe (CS) drill bit, while the second hole, H005, was drilled using a face bit (FB) drill bit. Hole H002 was cored 409–433 meters below seafloor (mbsf), using 10.5 ppg drilling mud as a lubricant (Figure 2). The core recovery was poor. The recovered sediment cores were divided into smaller sections based recovery quality. Core 4 was the only core collected under pressure, for in all other cores the pressure tool failed to close before leaving the gas hydrate stability zone.

H005 was cored at 284–287 mbsf and 417–450 mbsf, using seawater as a lubricant until switching to drilling mud at 435 mbsf. In both holes, gel sweeps were run during the coring process with a smectite based clay called bentonite in order to decrease the weight and increase the volume of the slurry. In Hole H005, the sediment was recovered in 13, 3 m long pressure cores (Figure 3). Many of the 3m cores were further divided into smaller sections based on core recovery and subsample needs. Cores 1 2, 3, 4, 7, 8, 10, 11, and 13 were collected under pressure. Cores 6 and 9 failed to pressurize. Overall core recovery in H005 was significantly better than H002 in both total length and successful pressurizations.

By analyzing the sediment composition in known gas hydrate reservoirs, we can construct a detailed picture of how and why gas hydrates accumulate, as mineralogy can affect sediment physical properties such as porosity and permeability as well as geophysical measurements such as resistivity. A sediment composed of clay minerals will have less pore space than that of a quartz based sediment. The spheroid grains of quartz do not fit so neatly together and therefore leave gaps for fluid accumulation and permeable movement. Moreover, mineralogical differences can influence measurements like resistivity logs. For example, clay minerals, with their high concentration of ions will increase conductivity, while minerals like quartz, an electrical insulator, increase resistivity.

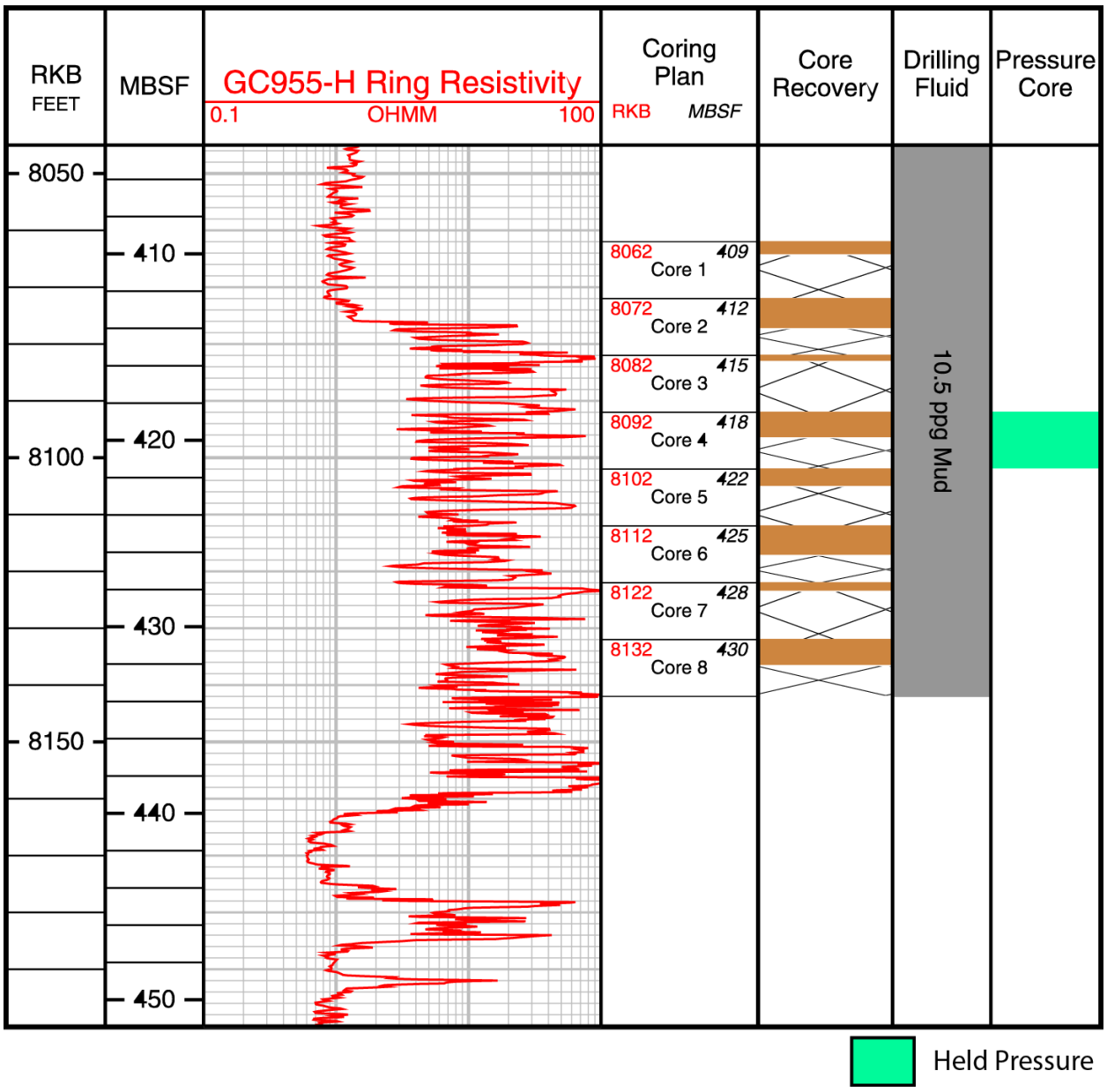

Figure 2. Core recovery and resistivity of Hole H002. Figure from Flemings et al. (2017, in preparation).

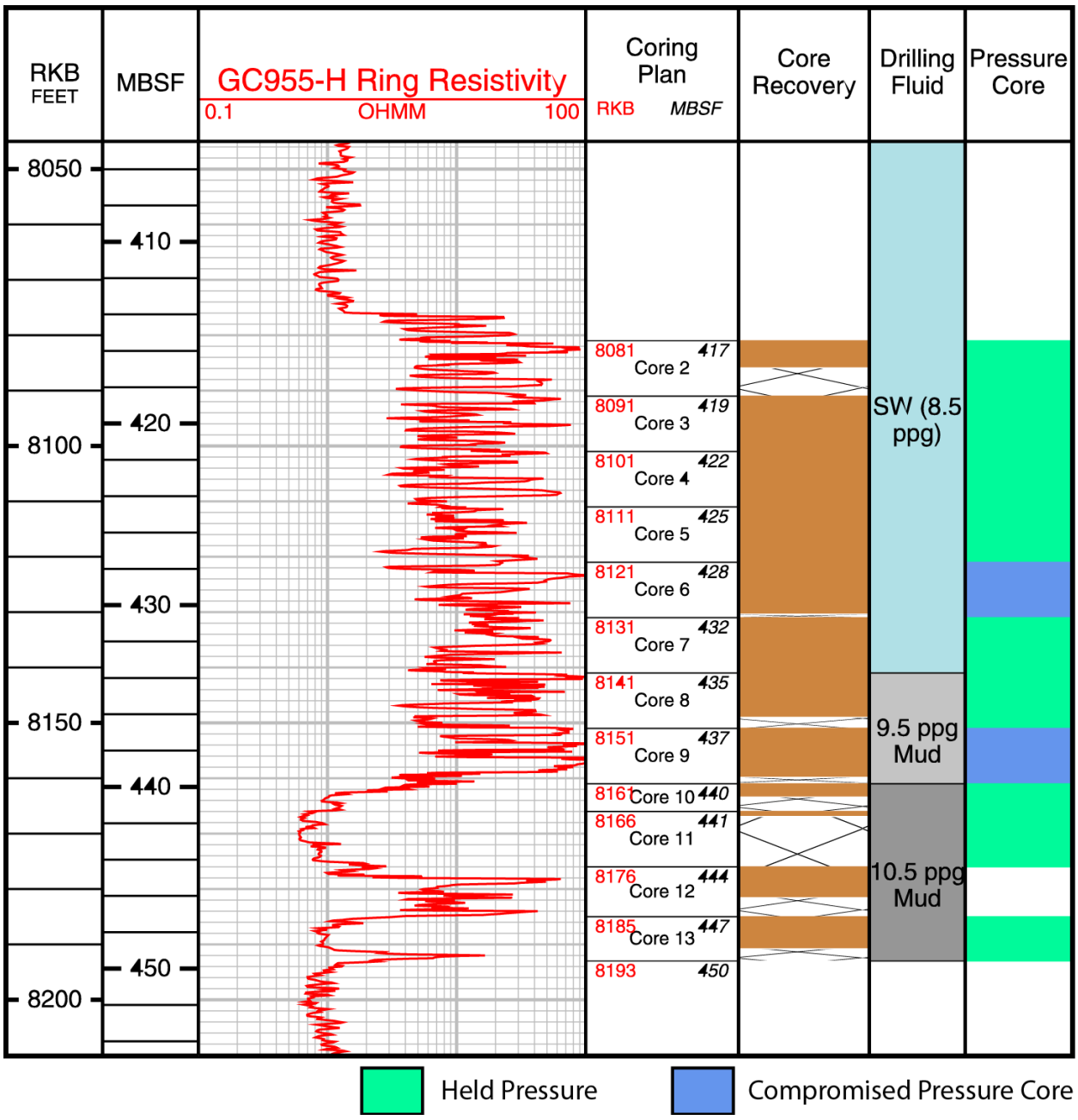

Figure 3. Core recovery and resistivity of Hole H005. Core 1 was collected in a shallower, fine-grained reservoir. Figure from Flemings et al. (2017, in preparation).

METHODS

XCT

Twenty-six non-pressurized core sections from both Holes H002 and H005 were scanned using an x-ray computed tomography (XCT) scanner at The Ohio State University. XCT, coupled with an image processing software (imageJ), provided a useful tool to image sediment core. High-resolution images were concatenated, creating a three dimensional representation of the sample without compromising its internal structure. The data could then be manipulated to provide qualitative visual analysis. XCT is largely sensitive to bulk density and the data is measured in Hondsfeild units (HU) in which air is given a value of -1000 and water is given a value of 0. Metals typically show values upwards of 2000 (Ketcham, 2001).

Subsampling

After scanning, the cores were split and subsampled for further analysis. One half of the split core was deemed the working half, used for subsampling, and the other half was photographed and archived. Cores with non-intact sediment were poured into bags.

Subsampling took place in silt intervals, denoted XRD-S, and drilling mud-intruded intervals, denoted XRD-M. Ten 2-gram subsamples, from both H002 and H005 cores, were collected. Moreover, eight subsamples (for a total of 18) from depressurized cores without drilling mud intrusion from H005 were sent to Ohio State from the University of Texas for XRD analysis. The subsamples were denoted using Lithofacies nomenclature (See Figure 5 and Table 1). A comparison between the two sets of subsamples will provide information on the degree of drilling mud influence. XRD-S is likely to correspond to Lithofacies 2 while XRD-M may resemble either Lithofacies 1 or 3, but such distinctions are not certain and are only used as a means of comparison.

Leica Microscope

Photomicrographs were acquired using a Leica DMS1000 digital light microscope. Both wet and dry subsamples taken from bagged sediment were imaged in order to obtain a fundamental qualitative sense of mineral assemblages before X-ray diffraction measurements were collected.

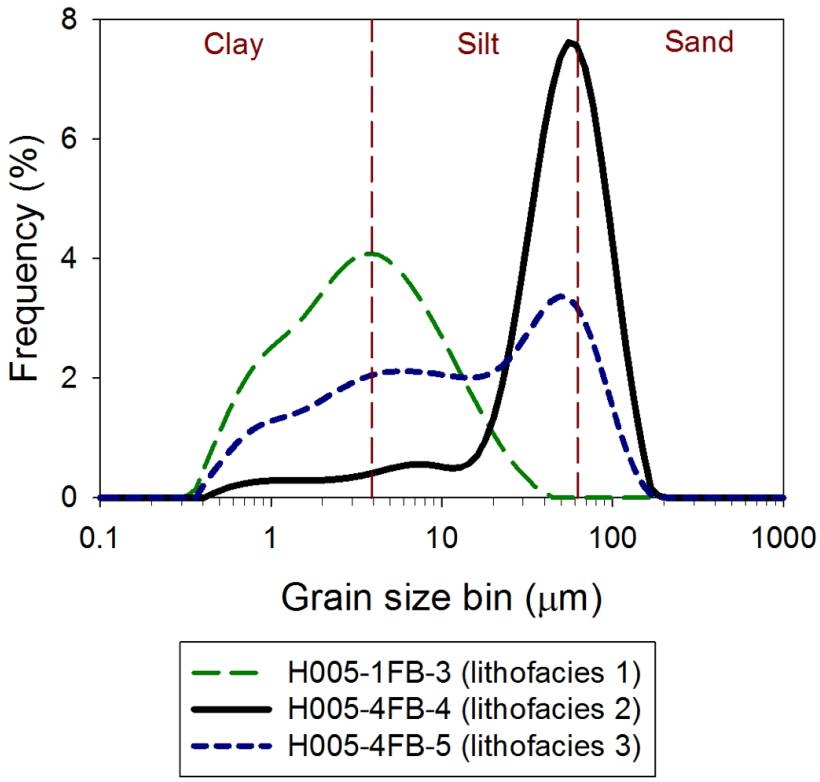

Figure 4. Grain size distribution of Lithofacies. Figure from Flemings et al. (2017, in preparation).

Table 1. Lithofacies nomenclature for subsamples from the University of Texas (Flemings et al. 2017, in preparation). Note that the P-wave velocity and hydrate saturation were collected on pressurized core.

Lithofacies	**Description**
Lithofacies 1	silty clay on average, characterized by a low P-wave velocity (~1600 m/s) and very low hydrate saturation (<3%)
Lithofacies 2	sandy silt with clay on average, characterized by high P-wave velocity (2800 – 3200 m/s) and very high hydrate saturation (60-90%)
Lithofacies 3	clayey silt with sand on average, characterized by lower P-wave velocities (1600-1800 m/s) and moderately low hydrate saturations (15 to 30%)
Fall in material	Sediment fell in from someplace above the borehole and does not look like intact core.

Table 2. Subsamples taken from Ohio State cores after splitting or bagging. Drilling mud intrusion may affect mineralogy.

Subsample	Type	Interval
H002-2CS-1	XRD-M	Bag
H002-3CS-1	XRD-S	17-18cm
H002-3CS-1	XRD-M	16-24cm
H002-6CS-3	XRD-S	Bag
H002-7CS-1	XRD-M	Bag
H002-8CS-3	XRD-S	Bag
H005-9FB-1	XRD-M	0-1cm
H005-9FB-4	XRD-M	0-7cm
H005-12FB-3	XRD-S	33-34cm
H005-12FB-3	XRD-M	27-31cm

Table 3. Subsamples sent to Ohio State University from the University of Texas. No drilling mud intrusion.

Subsample	**Lithofacies**
H005-1FB-1	Fall in material
H005-1FB-2	Fall in material
H005-1FB-3	Lithofacies 1
H005-2FB-1	Fall in material
H005-3FB-3	Lithofacies 2
H005-4FB-3	Lithofacies 3
H005-4FB-4	Lithofacies 2
H005-9FB-4	Multiple/uncertain

XRD

X-ray diffraction measurements were collected using a PANalytical X'pert Pro X-ray diffractometer to determine the bulk mineralogy. Preparation included drying and grinding 2 grams of sediment into a fine powder with a corundum mortar and pestle, and back-loading it into a stainless steel cavity mount. Cu K-alpha radiation with a wavelength of 0.15418 nm was the incident radiation directed at the sample, and the diffracted (reflected) intensities off crystal planess were measured. A peak intensity occurs when diffracting planes in a crystal are oriented such that the 2-theta angle of the incident X-ray beam satisfies Bragg's Law ($n\lambda=2d\sin\theta$). The inter-planar spacing (d-spacing) that coincides with each measured 2θ reflection for the particular plane (hkl) was calculated. The subsequent data were processed with the analytical software platform Highscore Plus along with the PDF 4+ mineral database in order to identify the minerals present based on diffraction peak patterns from the database.

The Rietveld Method, which models the full experimental pattern with a least squares residual approach was used to convert observed and calculated peak intensities into mineral weight percentages in order to provide a semi-quantitative estimate of mineral abundance (Rietveld, 1969). S scale factors and unit cell parameters were among the parameters allowed to vary during Rietveld refinement. Profile fits were adjusted based on experimental scan characteristics, and the initial qualitative mineral results were modified by selecting only high quality database patterns with structural data included. H002-3CS-1 (XRD-M), H005-12FB-3 (XRD-S), H005-1FB-3 (Lithofacies 1), H005-3FB-3 (Lithofacies 2), and H005-4FB-3 (Lithofacies 3) were chosen for as representative samples for refinement for each sediment category.

RESULTS

XCT

The XCT scans of Ohio State cores show bright high-density areas greater than 5000 Hounsfield units both along the edges of the cores and interbedded within the sediment. These areas were targeted for subsampling and placed into the XRD-M category. Few structures were observed in the XCT scans due to poor core quality and the disruptive intrusion of the drilling mud.

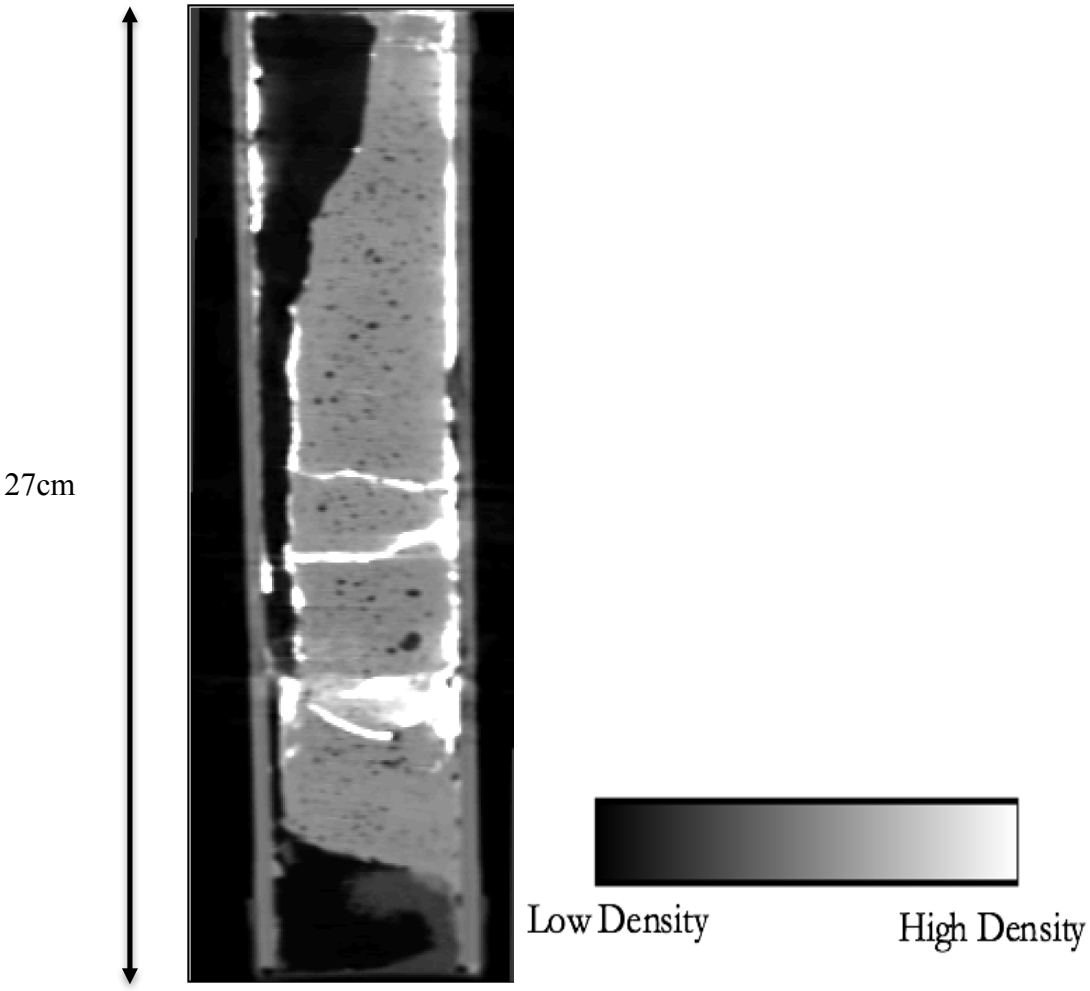

Figure 5. XCT slab view image of H002-3CS-1. Bright sections along liner and interbedded in sediment indicate high-density material that is most likely barite based drilling mud

Leica Images

Leica images reveal an abundance of spherical conchoidal minerals deemed to be quartz (Figure 6). Cleavage planes characteristic of both feldspars and micas are also visible. A smattering of black minerals (likely amphibole) stands out from the rest of the sediment (Figure 7). A subtle greenish tint can be noticed in sections of the sediment, which suggests the presence of chlorite. Moreover, some images taken from Ohio State subsamples show a matrix with a dull metallic

luster filling the space between grains in an amorphous pattern. Drilling mud intrusion is thought to be the contributing factor to this observation.

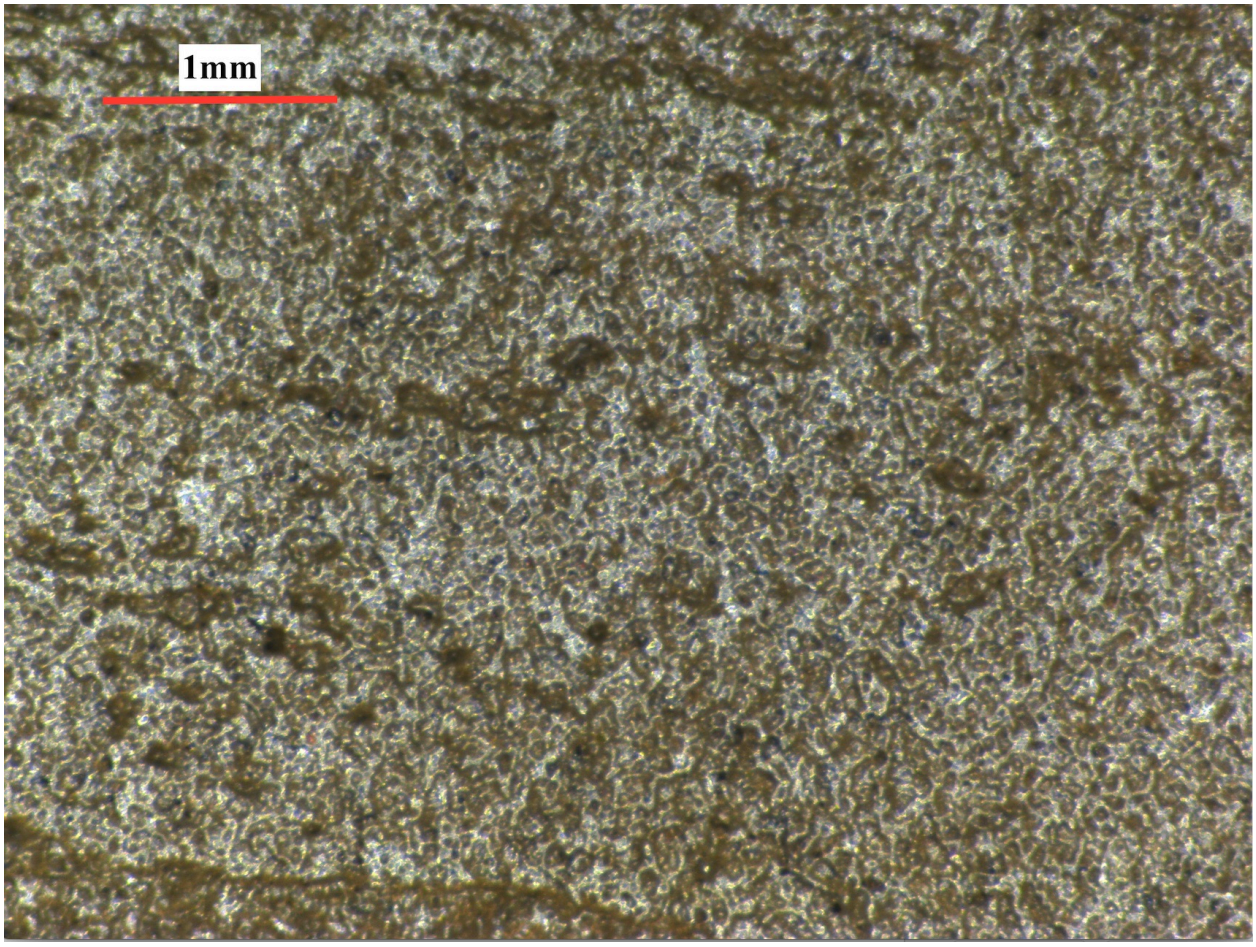

Figure 6. Leica microscope image of H002-7CS-1. Note grey metallic fluid between grains is likely drilling mud.

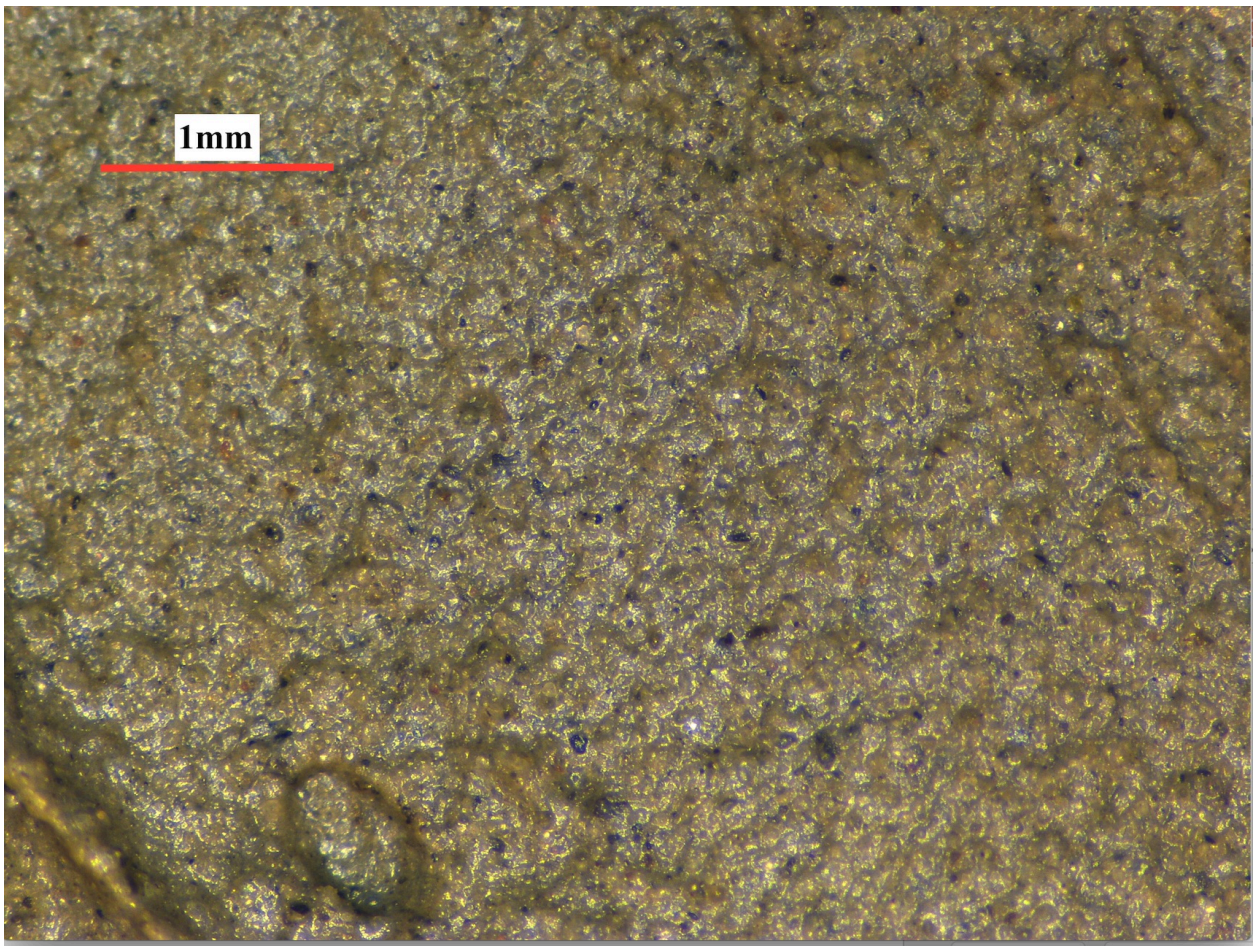

Figure 7. Leica microscope image of H002-2CS-1. Note black minerals are likely amphibole.

Qualitative XRD

XRD-S samples show a composition of mainly quartz with minor amounts of feldspars, amphibole, muscovite, dolomite, calcite and clays, including kaolinite, chlorite and serpentine based on 7 and 14 angstrom reflections (see Appendix). The identification of clay minerals can be challenging due to slight differences in chemistry, polytype, and degree of order, which create many possible permutations of phyllosilicate structures. Moreover, interlayered smectite may be responsible for a broadened 14.8 angstrom peak observed across multiple samples. The dulled resolution makes specific identification burdensome, and further sample preparation involving clay separation and solvation would be necessary to distinguish the differences in clay mineralogy. Similar problems arise when differentiating between potassium feldspar structural states.

XRD-M samples show a similar composition including quartz, feldspars, amphibole, muscovite, dolomite, and calcite but with the addition of barite (a component used in drilling mud and a high density mineral). Subsamples H002-3CS-1 and H005-12FB-3 included barite in significant quantities, matching the presence of high-density bright spots in their respective XCT scans.

University of Texas subsamples also showed a predominantly quartz composition, with feldspars, calcite, dolomite, amphiboles, micas, and clays all making an appearance. Lithofacies 2 had fewer clay minerals than Lithofacies 1 and 3. A wide band low intensity 2.72 angstrom peak, observed in University of Texas subsamples, is suggestive of pyrite, but there is not enough evidence to confirm that claim. All samples contained quartz, calcite, dolomite, albite, and muscovite.

Table 4. Qualitative mineral composition of all XRD Subsample

Subsample	Type/facies	Quartz	Calcite	Dolomite	Chlorite-Serpentine	Orthoclase	Albite	Microcline	Muscovite	Biotite	Richterite	Magnesio-hornblende	Kaolinite	Vermiculite	Clinochlore	Clinochrysotile	Talc	Barite
H002-2CS-1	XRD-M	✔	✔	✔	✔	✔	✔		✔	✔		✔	✔					
H002-3CS-1	XRD-S	✔	✔	✔			✔	✔	✔		✔				✔	✔		
H002-3CS-1	XRD-M	✔	✔	✔			✔	✔	✔		✔			✔	✔			✔
H002-6CS-3	XRD-S	✔	✔	✔	✔		✔	✔	✔			✔	✔	✔				
H002-7CS-1	XRD-M	✔	✔	✔	✔	✔	✔		✔			✔	✔	✔				
H002-8CS-3	XRD-S	✔	✔	✔	✔		✔	✔	✔			✔						
H005-9FB-1	XRD-M	✔	✔	✔	✔		✔	✔	✔	✔		✔	✔	✔				
H005-9FB-4	XRD-M	✔	✔	✔			✔	✔	✔			✔	✔	✔				
H005-12FB-3	XRD-S	✔	✔	✔	✔		✔	✔	✔			✔	✔	✔				
H005-12FB-3	XRD-M	✔	✔	✔	✔		✔	✔	✔			✔	✔					✔
H005-1FB-1	Fall in material	✔	✔	✔	✔		✔	✔	✔			✔	✔					
H005-1FB-2	Fall in material	✔	✔	✔	✔		✔	✔	✔			✔	✔	✔				
H005-1FB-3	Lithofacies 1	✔	✔	✔	✔		✔	✔	✔	✔		✔	✔	✔				
H005-2FB-1	Fall in material	✔	✔	✔	✔		✔	✔	✔	✔		✔	✔					
H005-3FB-3	Lithofacies 2	✔	✔	✔	✔		✔		✔	✔		✔						
H005-4FB-3	Lithofacies 3	✔	✔	✔	✔	✔	✔		✔			✔		✔				
H005-4FB-4	Lithofacies 2	✔	✔	✔	✔		✔	✔	✔			✔		✔			✔	
H005-9FB-4	Multiple/uncertain	✔	✔	✔			✔	✔	✔			✔			✔			

Quantitative XRD

Quantitative results from Rietveld refinement reveal a predominantly quartz based sediment with significant quantities of feldspars and carbonate, and minor quantities of micas, amphiboles, and clays (Figures 8–12). Quartz was the largest percentage in each subsample (24.0–46.8%), followed by albite (17.1–25.8%). Carbonates (calcite and dolomite) combined for a range of 13.3–24.3% across samples. Micas, both muscovite and biotite, made up 2.2–10.1%. Amphiboles accounted for 2–5.4%. Lastly, clay minerals including vermiculite, kaolinite and chlorite contributed 1.2–11%.

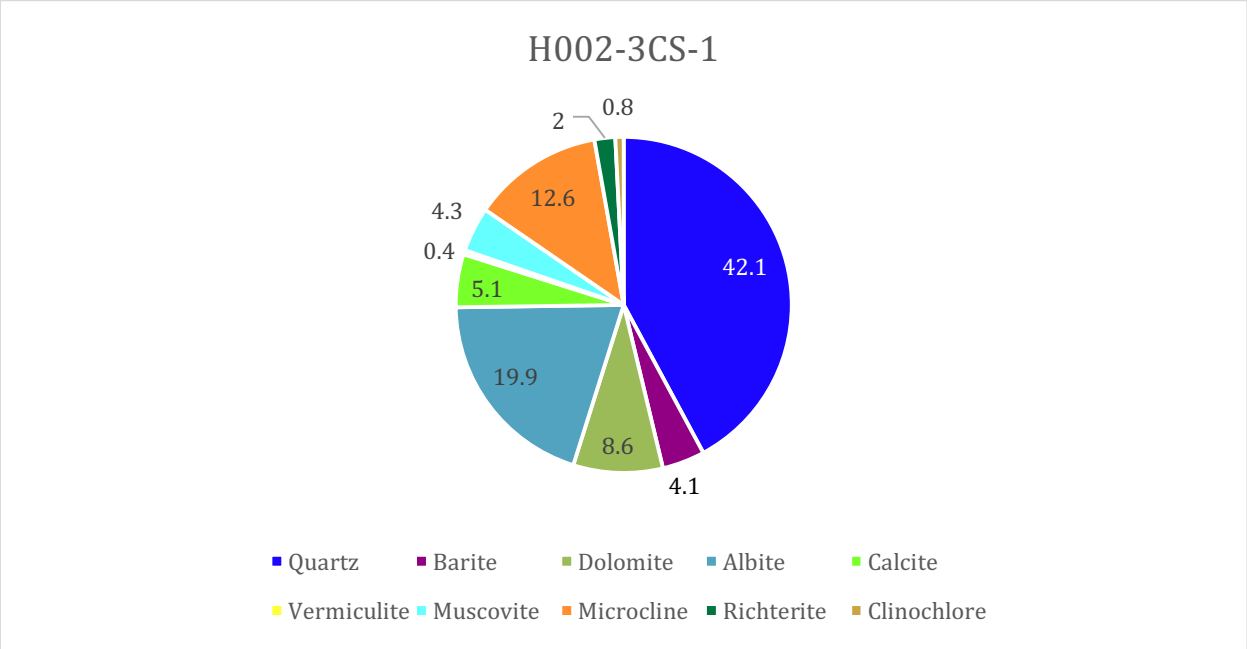

Figure 8. Rietveld refinement results of H002-3CS-1 (XRD-M)

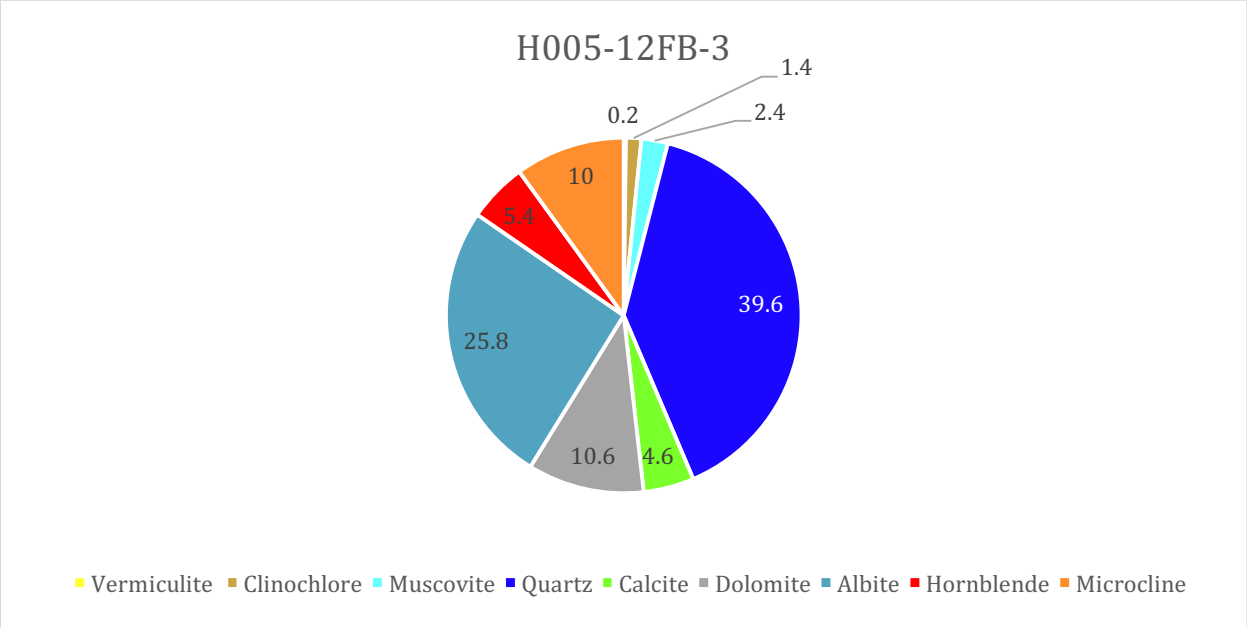

Figure 9. Rietveld refinement results of H005-12FB-3 (XRD-S)

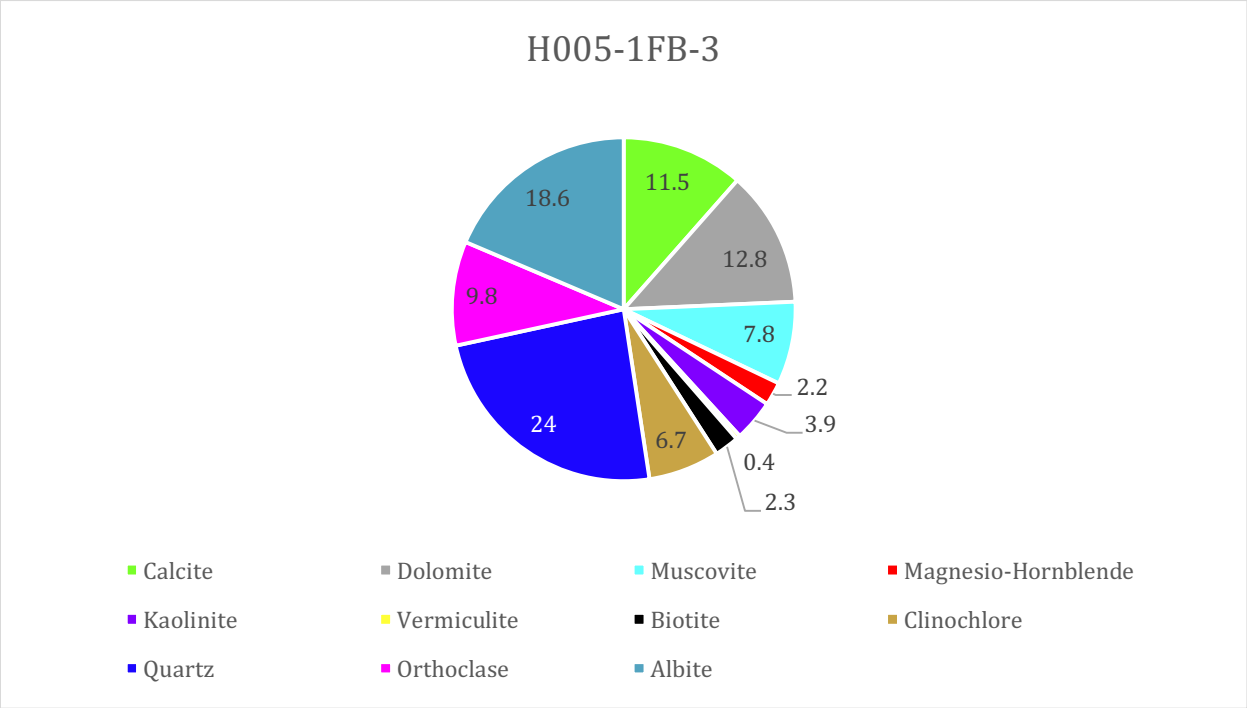

Figure 10. Rietveld refinement results of H005-1FB-3 (Lithofacies 1)

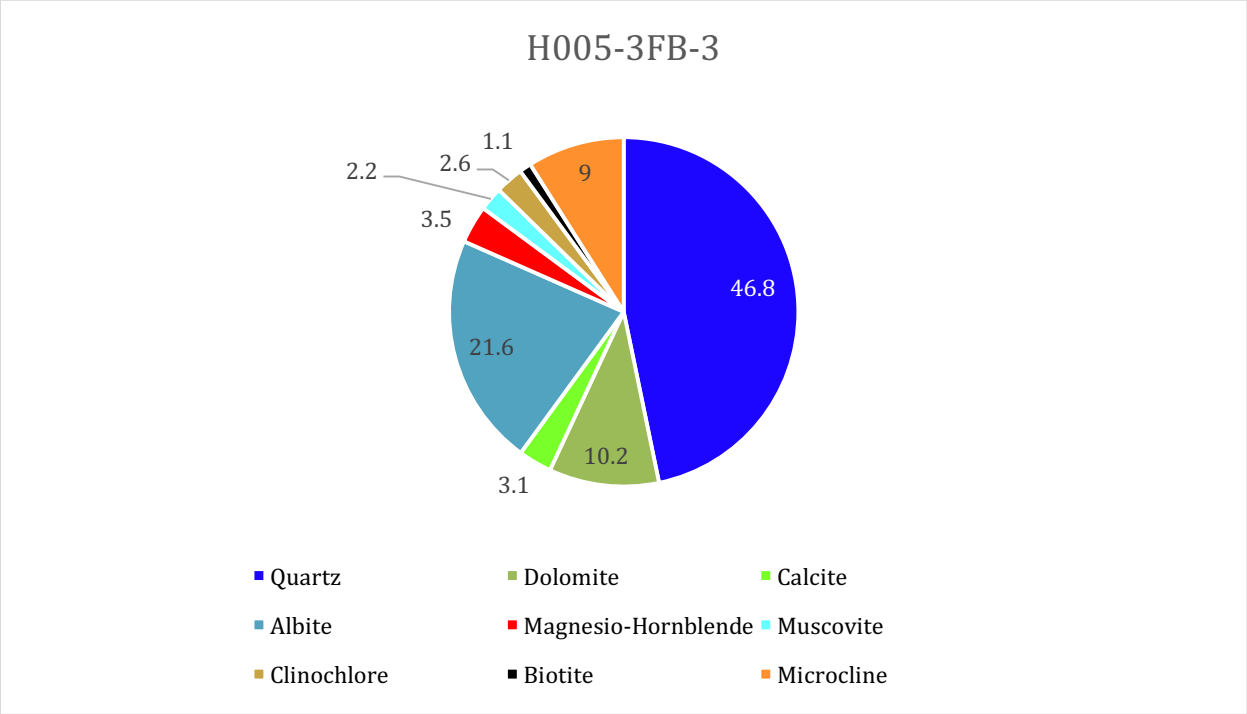

Figure 11. Rietveld refinement results of H005-3FB-3 (Lithofacies 2)

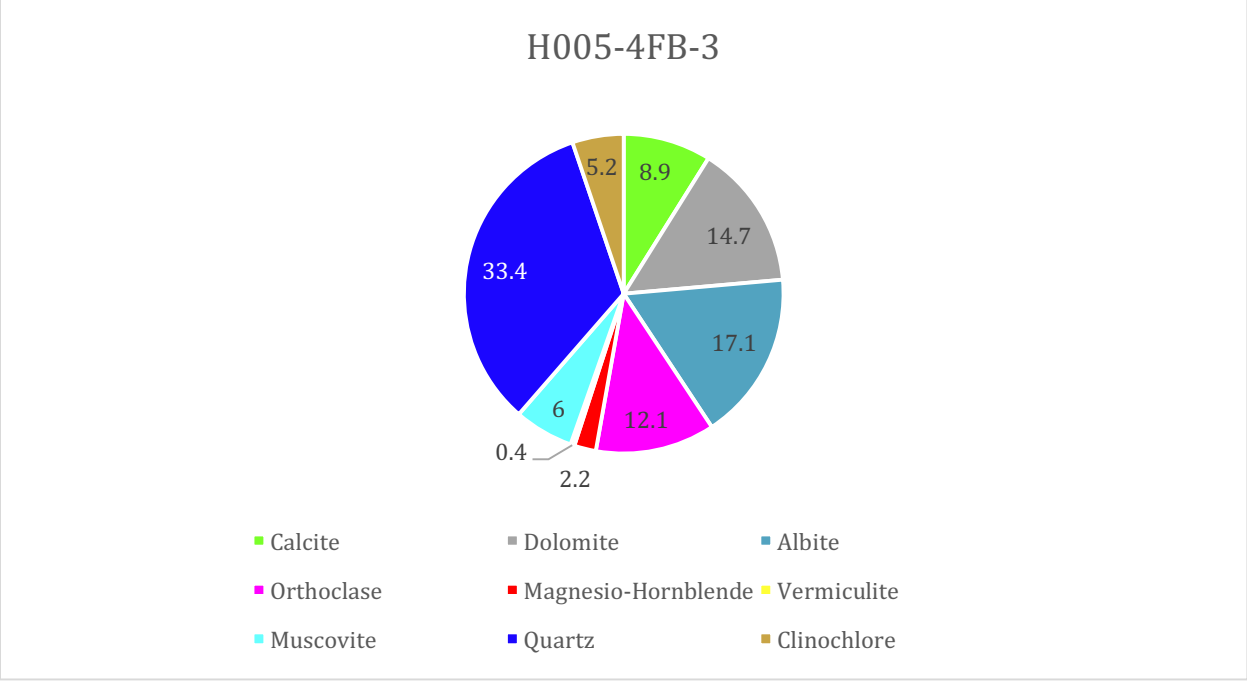

Figure 12. Rietveld refinement results of H005-4FB-3 (Lithofacies 3)

In addition to mineral abundances, the software calculated agreement indices in order to illustrate the accuracy of results. The R expected denoted the best possible residual value; a low value (less than 5%) indicates high quality data. The R profile and weighted R profile indicate quality matches between collected and modeled data. Values less than 10% are particularly robust. Lastly, the goodness of fit is the ratio of weighted R and expected R. Subsamples from University of Texas cores generally had better agreement indices than those from Ohio State cores.

Table 5. Agreement indices for quality of Rietveld refinement.

Subsample	Type	R expected	R profile	Weighted R profile	Goodness of Fit
H002-3CS-1	XRD-M	4.706	20.414	29.254	38.647
H005-12FB-3	XRD-S	4.373	23.934	33.005	56.972
H005-1FB-3	Lithofacies 1	4.400	7.760	9.941	5.102
H005-3FB-3	Lithofacies 2	4.637	18.283	25.991	31.423
H005-4FB-3	Lithofacies 3	4.236	11.068	15.045	12.616

Discussion

Qualitative Mineral Identification

I am confident in my mineral selections based on evidence from Leica images and peak intensity phase identification. Quartz is clearly identified by its conchoidal fracture, feldspars and micas by their cleavage planes. Kaolinite can be justified as a part of the mineral assemblage due to the presence of feldspar minerals of which kaolinite is a chemically weathered product. Specific peak intensities are characteristic of certain minerals. For example, the 14.7 angstrom peak observed in the XRD data is distinctive of vermiculite, the 8.3 points to amphibole, and peaks around 7 angstroms to chlorite minerals (see Appendix).

The widened 14.8 angstrom peak may be a product of the bentonite gel sweeps run in both H002 and H005 (see Appendix). This intensity pattern was observed across multiple samples, and an XRD measurement of the both the drilling mud and gel would be needed to subtract any unnatural signals and obtain a true profile of the sediment. Despite complications, we were able to construct qualitative results that matched visual observations to instrument measured data, thus providing a stronger case for our derived mineral assemblages.

Quantitative Analysis

H005-1FB-3, representative of Lithofacies 1, consisted of the most clay minerals (11%), while H005-3FB-3, representing Lithofacies 2, had the least (1.1%). The Lithofacies 3, H005-4FB-3, fell somewhere in the middle (5.6%). These results match grain size distributions created by the University of Texas (Figure 4) in which Lithofacies 1 contains the most clay sized grains and Lithofacies 2 contains the most silt to sand sized grains (Lithofacies 3 falling somewhere between them). Moreover, the mineralogy of Lithofacies 2 is consistent with its 60–90% hydrate saturation. The lack of clay minerals allows for a larger and more connected pore spaces, while Lithofacies 1, with its abundant clay minerals, had less than 3% hydrate saturation. Coarse-grained quartz abundant reservoirs with minimal clay are ideal for high hydrate saturation.

Drilling Mud Intrusion

Cores drilled with 10.5 pounds per gallon (ppg) mud experienced some level of contamination due to drilling mud intrusion, illustrated by the presence of barite in XRD scans (see Table 4 and Appendix) and the high density bright spots observed in XCT scans (Figure 5). Mud intrusion disturbed the sediment and compromised stratigraphic information and structures. Based on R profile values (Table 5), Ohio State mud contaminated subsamples showed a larger degrees of error than University of Texas subsamples. Clearly, mud intrusion also compromised the accuracy of quantitative results by further complicating an already complex multi-phase intensity pattern, Even cores drilled with seawater in Hole H005 may have experienced some level of contamination due to bentonite gel sweeps that take place during the drilling process.

Rietveld Semi-Quantitative Error

It is important to emphasize the semi-quantitative nature of all Rietveld refinement results. Although the method is able to calculate relative abundances of minerals, sources of error are

endemic to each step of the process including but not limited to sample preparation, intensity measurement, and instrumentation. Successful application of the method could lead to up to 30% differences with independent determinations using petrographic microscopes (Connolly, 2012). Accurate quantitative analysis is especially difficult in multi-phase clay bearing sediment. Nonetheless, the bulk mineralogical assemblages presented in the results still hold significance for gas hydrate reservoirs in spite of the inherent errors associated with their collection.

The refinement matched observed and expected data for minerals like calcite and barite with great accuracy. However, I observed an under-estimation of quartz and an over-estimation of albite (Figures 15 and 16). Based on Leica images, we expected higher percentages of quartz, so the samples are likely more abundant in SiO_2 then calculated. The percentage difference is accounted for by inflated albite percentages.

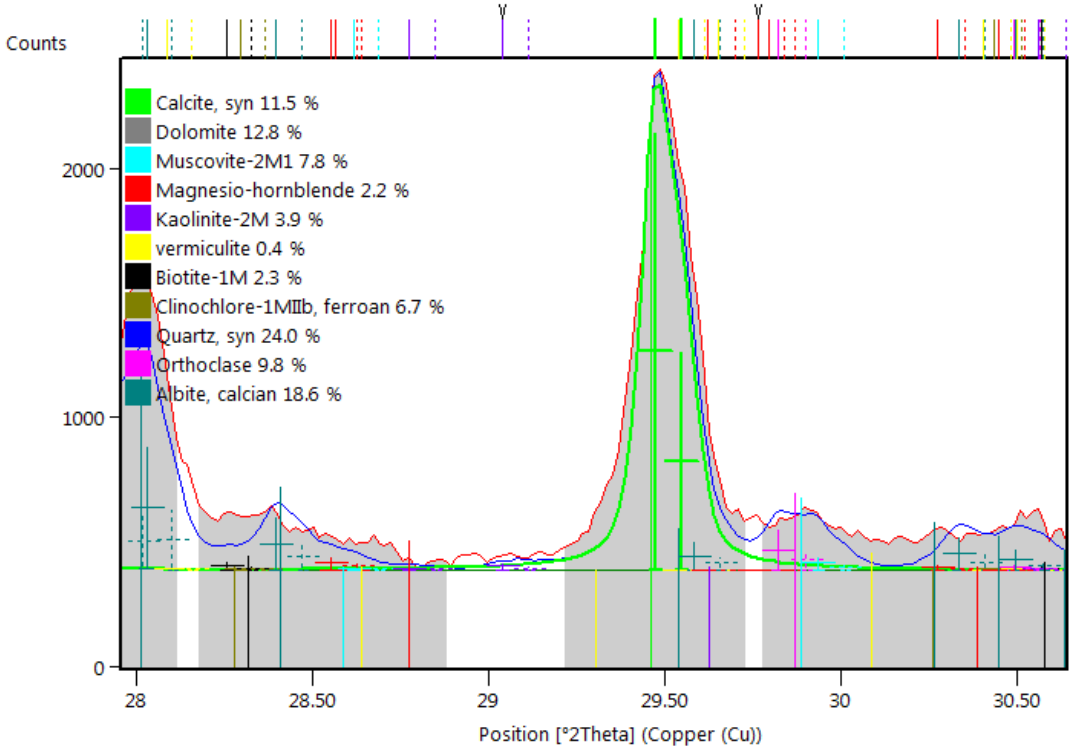

Figure 13. A calcite peak with observed and calculated intensities matching well from sample H005-1FB-3 (Lithofacies 1).

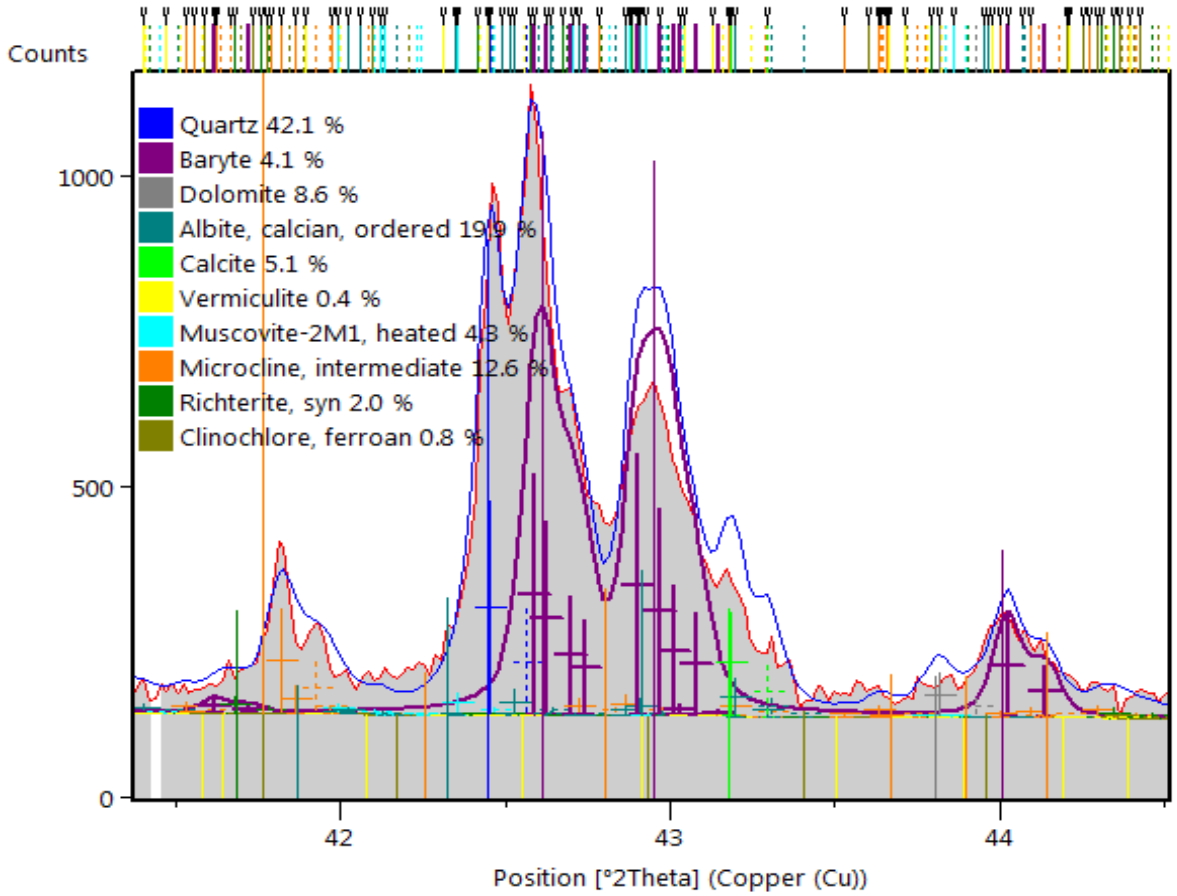

Figure 14. Barite peaks with observed and calculated intensities matching well from sample H002-3CS-1 (XRD-M).

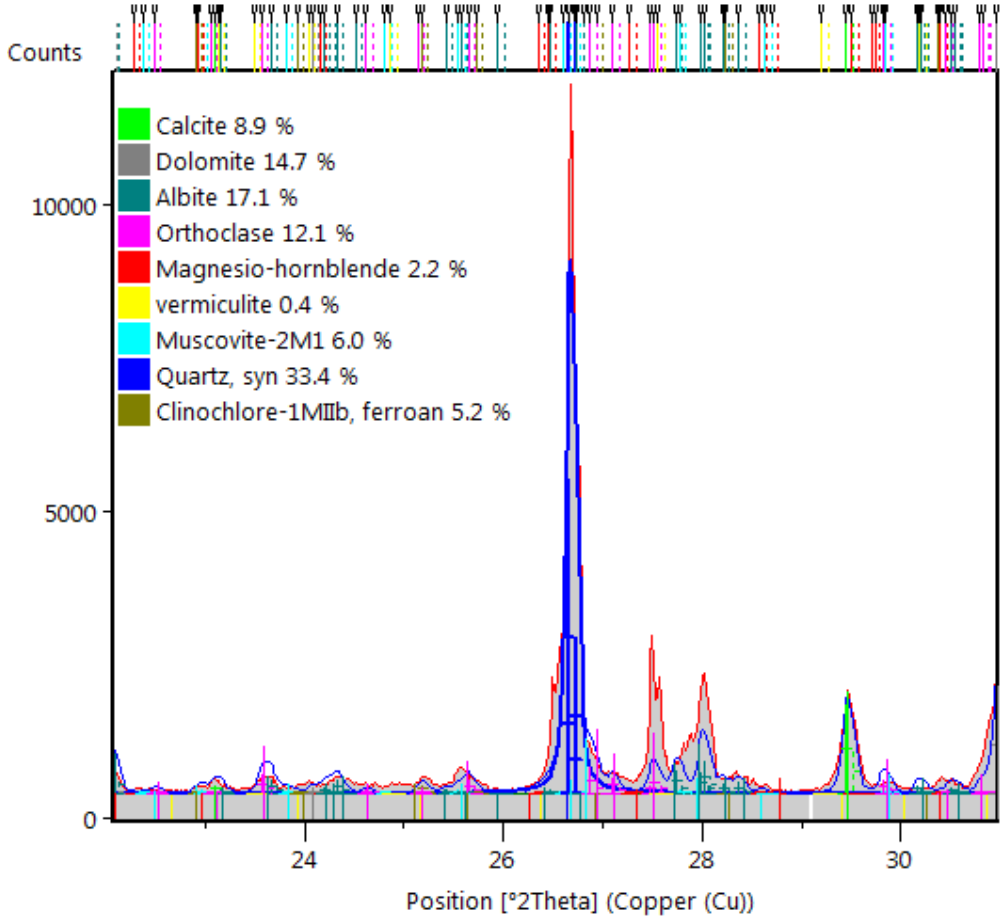

Figure 15. A calculated underestimation of a quartz peak compared to its observed intensity from sample H005-4FB-3 (Lithofacies 3)

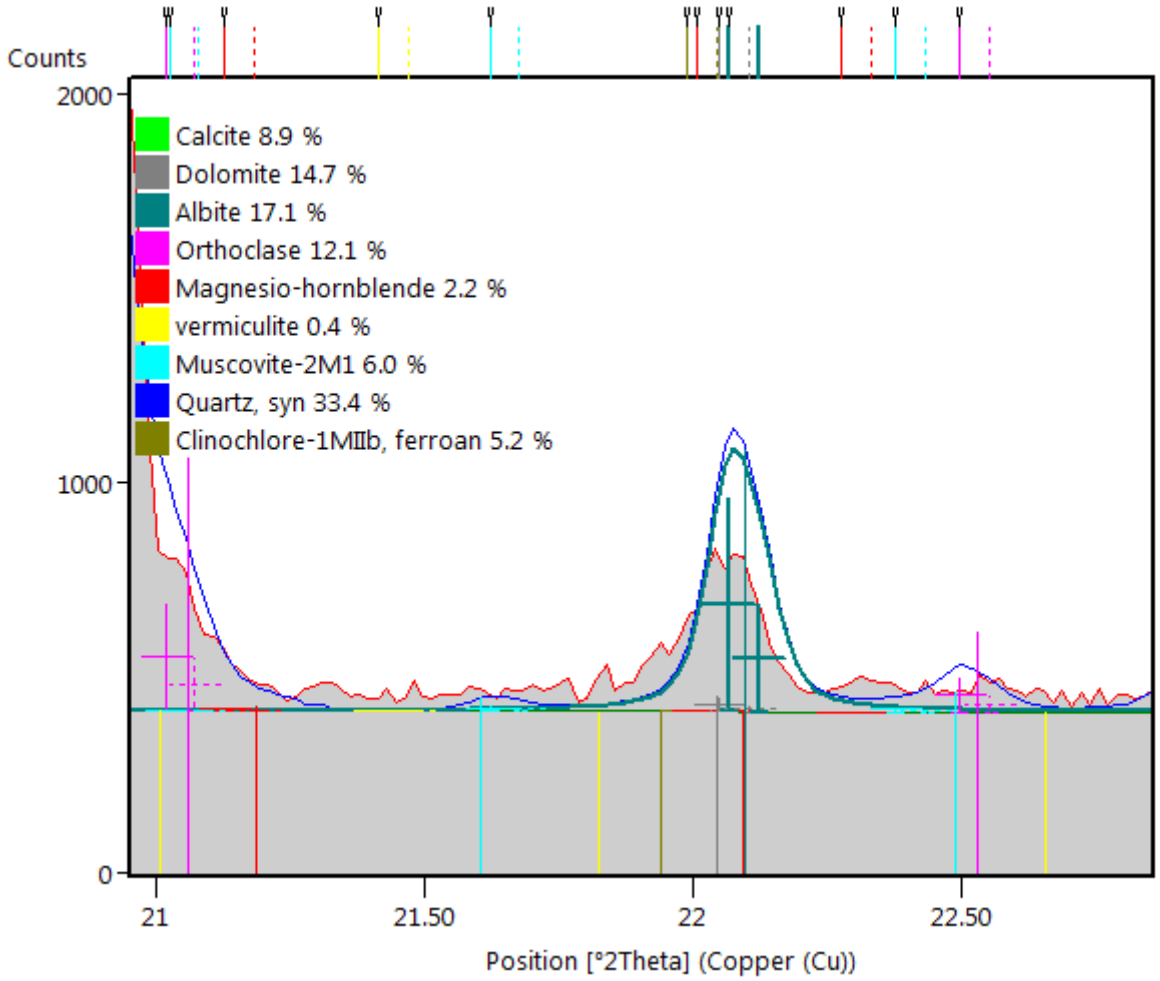

Figure 16. A calculated overestimation of an albite peak compared to its observed intensity form sample H005-4FB-3 (Lithofacies 3)

CONCLUSIONS

Natural gas hydrate reservoirs, with their promising energy prospectus, will continue to play a pivotal role in geoscience research. Therefore, describing the physical characteristics and conditions that lead to highly saturated accumulations, will be paramount in constructing any meaningful future appropriation strategy. A fundamental understanding of gas hydrate reservoirs is sought through investigations at the mineralogical scale, breaking down a 100m thick unit into its smaller building blocks. The highest hydrate-saturated section of the Green Canyon Block 955 reservoirs is a quartz rich, clay poor sediment, with sufficient effective pore space to allow for the accumulation of gas hydrate.

Drilling mud intrusion, affecting the integrity of XCT and XRD data demonstrated how the muds and gels necessary for core acquisition can imprint themselves onto the native sediments and compromise data. Qualitative results likely reflect a combination of mud, gel, and sediment.

Although semi-quantitative methods provide valuable information regarding proportionality, hesitation must outweigh any desire to attribute conclusively to such results, but instead, a careful analysis of how quantitative measurements compare to the broader background of collected data. For example, quartz percentages were largest in Lithofacies 2, but with a multiphase sample, the exact mineral proportions are beyond the capabilities of Rietveld refinement due to error. Nonetheless these result still provide insight into the characteristics of the sediment, especially when evaluated alongside grain size distributions and gas hydrate saturation.

RECOMMENDATIONS FOR FUTURE WORK

Analysis of our sediment using the scanning electron microscope (SEM) would allow for a more precise differentiation between clay minerals. Specifically, differences between muscovite and illite and differences between biotite and vermiculite would be identified. With better qualitative results, a more robust quantitative profile can be achieved. Moreover, using an internal corundum standard of known weight percent may improve the quantitative results. Distinguishing clay minerals can also be accomplished through separating preparation techniques prior an XRD analysis. If the clay minerals are isolated, the peak intensity profile will be less convoluted and therefore easier to decipher. Lastly, we recommend an XRD analysis of both the drilling mud and bentonite gel used and the UT-GOM2-01 in order to determine the background signal that may be imprinting on the sediment samples.

REFERENCES CITED

Armstrong-Altrin, J.S., and Machain-Castillo, M.L., 2016, Mineralogy, geochemistry, and radiocarbon ages of deep sea sediments from the Gulf of Mexico, Mexico: Journal of South American Earth Sciences, v. 71, p. 182-200.

Arora, A., Cameotra, S.S., Kumar, R., Balomajumder, C., Singh, A.K., Santhakumari, B., Kumar, P., and Laik, S., 2016, Biosurfactant as a promoter of methane hydrate formation: thermodynamic and kinetic studies: Scientific Reports, v. 6, p. 20893.

Buffett, B., 11, 2004, Global inventory of methane clathrate: sensitivity to changes in the deep ocean: Earth and Planetary Science Letters, v. 227, p. 185; 185-199; 199.

Burwicz, E., 2017, 3-D basin-scale reconstruction of natural gas hydrate system of the Green Canyon, Gulf of Mexico MODELING OF THE GREEN CANYON GAS HYDRATE: Geochemistry, Geophysics, Geosystems: G3, v. 18, p. 1959; 1959-1985; 1985.

Collett, T.S., Lee, M.W., Zyrianova, M.V., Mrozewski, S.A., Guerin, G., Cook, A.E., and Goldberg, D.S., 2012, Gulf of Mexico Gas Hydrate Joint Industry Project Leg II logging-while-drilling data acquisition and analysis: Marine and Petroleum Geology, v. 34, p. 41-61.

Connolly, J.R., 2012, Introduction Quantitative X-Ray Diffraction Methods for EPS400, University of New Mexico: http://epswww.unm.edu/media/pdf/09-Quant-intro.pdf (accessed October 2017).

Devine, S.B., 1971, Mineralogical and geochemical aspects of the surficial sediments of the deep Gulf of Mexico [Ph.D. thesis]: Louisiana State University.

Frederick, J.M., and Buffett, B.A., 2016, Submarine groundwater discharge as a possible formation mechanism for permafrost-associated gas hydrate on the circum-Arctic continental shelf: Journal of Geophysical Research: Solid Earth, v. 121, p. 1383-1404, doi: 10.1002/2015JB012627.

Flemings, P.B., Phillips, S.C., Collett, T., Cook, A., Boswell, R and the UT-GOM2-Expedition Scientists (2017, in preparation) UT-GOM2-1 Hydrate Pressure Core Expedition Report. Available through UT-Austin.

Haines, S.S., Hart, P.E., Collett, T.S., Shedd, W.W., and Frye, M., 2015, High-resolution seismic imaging of the gas and gas hydrate system at Green Canyon 955 in the Gulf of Mexico: American Geophysical Union Fall Meeting, v. 2015, p. @AbstractOS23D-06.

Ketcham, R.A., 2001, Acquisition, optimization and interpretation of X-ray computed tomographic imagery; applications to the geosciences: Computers & Geosciences, v. 27, p. 381; 381-400; 400.

Kvenvolden, K.A., 1993, Gas hydrates-geological perspective and global change: Reviews of Geophysics , v. 31, p. 173; 173-187; 187.

McConnell, D., Boswell, R., Colle, T., Frye, M., Shedd, W., Guerin, G., Cook, A., Mrozewski, S., Dufrene, R., and and Godfriaux, P., 2009, Gulf of Mexico Gas Hydrate Joint Industry Project Leg II: Green Canyon 955 Site Summary.

Milkov, A.V., Sassen, R., Novikova, I., and Mikhailov, E., 2000, Gas hydrates at minimum stability water depths in the Gulf of Mexico: significance to geohazard assessment: Gulf Coast Association of Geological Societies, v. 50, p. 217-224.

Rietveld, H., 1969, A profile refinement method for nuclear and magnetic structures: Journal of Applied Crystallography, v. 2, p. 65-71.

Rogers, R.E., and Lee, M., Biosurfactant from microbial activity in ocean sediments enhances gas hydrate formation, *in* Geological Society Earth System Processes-Global Meeting, Sponsored jointly by the Geological Society of London and Geological Society of America, Edinburgh, Scotland, June, p. 24-28.

Ruppel, C., 2007, Tapping methane hydrates for unconventional natural gas: Elements, v. 3, p. 193-199.

Ruppel, C.D., Kessler, J.D., 2016, The interaction of climate change and methane hydrates Climate-Hydrates Interactions: Reviews of Geophysics, v. 55, p. 126; 126-168; 168.

Sloan Jr, E.D., and Koh, C., 2007, Clathrate hydrates of natural gases: CRC press, p. 47.

Zhong, Y., and Rogers, R.E., 2000, Surfactant effects on gas hydrate formation: Chemical Engineering Science, v. 55, p. 4175-4187.

APPENDIX

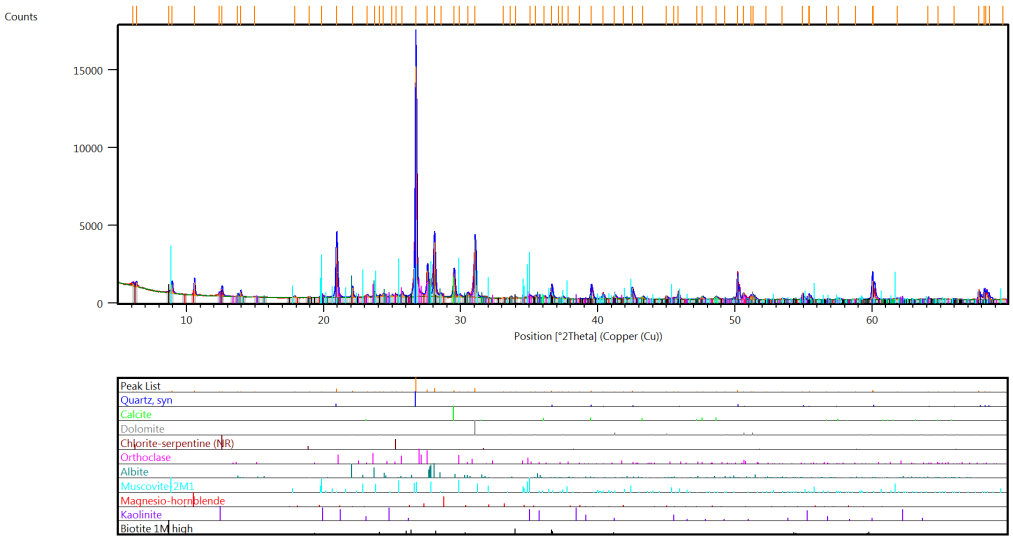

Figure A1. H002-2CS-1 phase ID

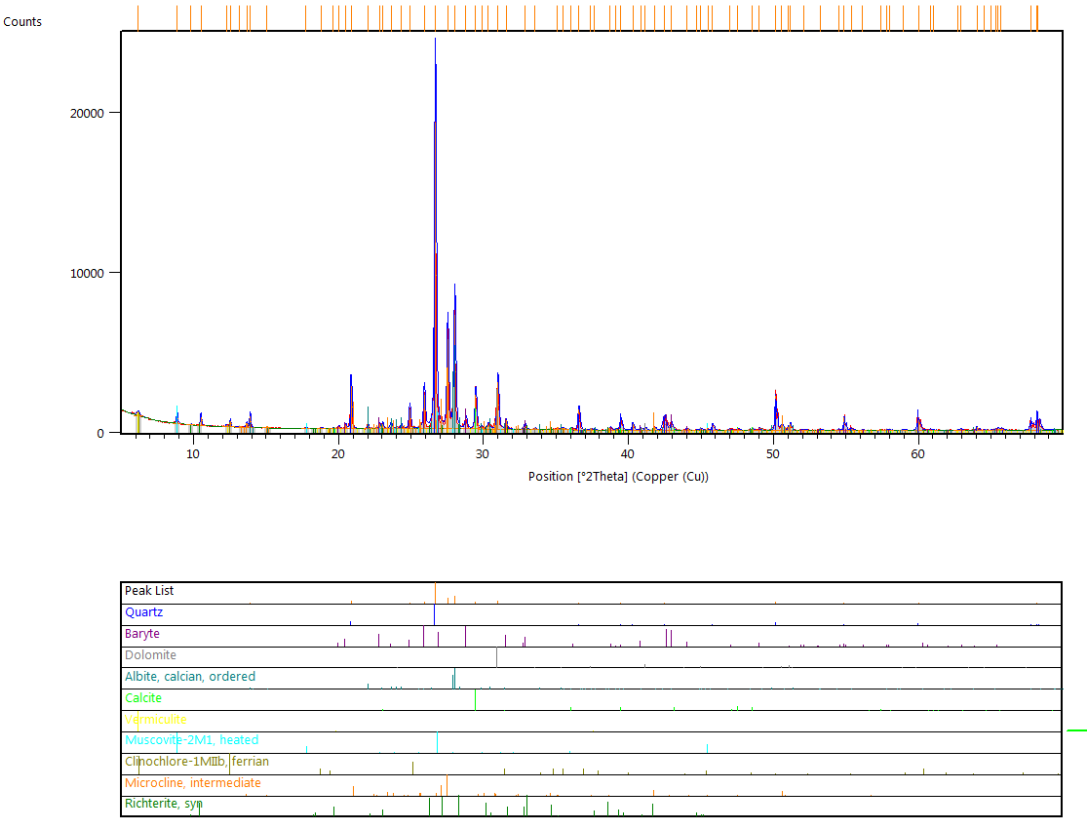

Figure A2. H002-3CS-1 phase ID

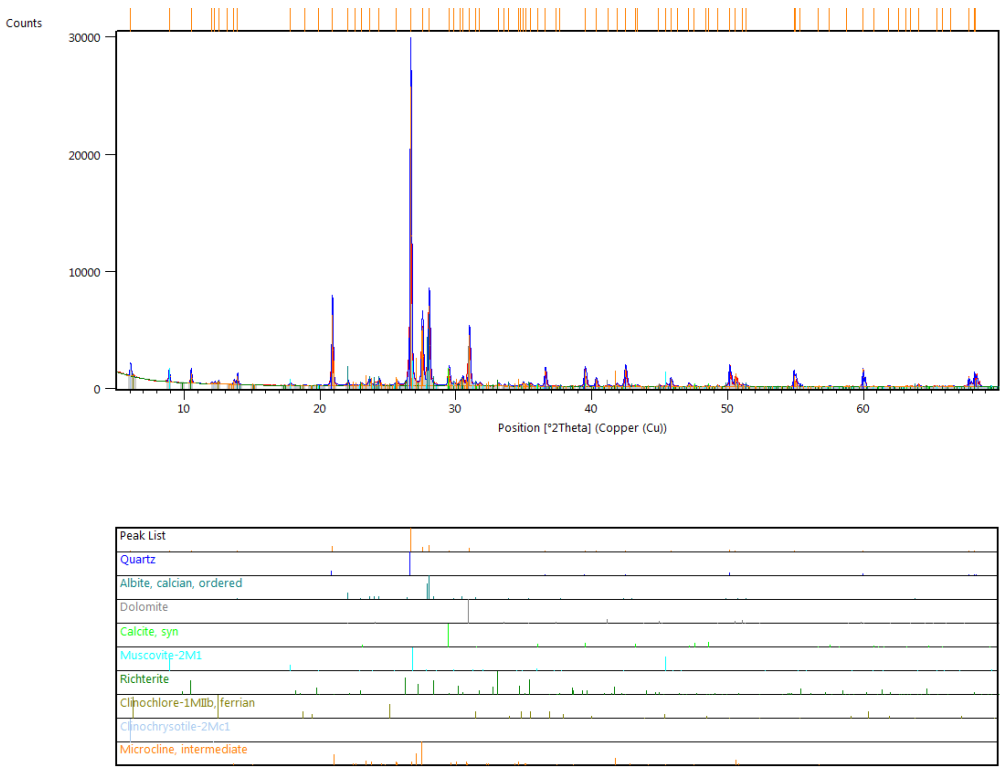

Figure A3. H002-3CS-1 phase ID

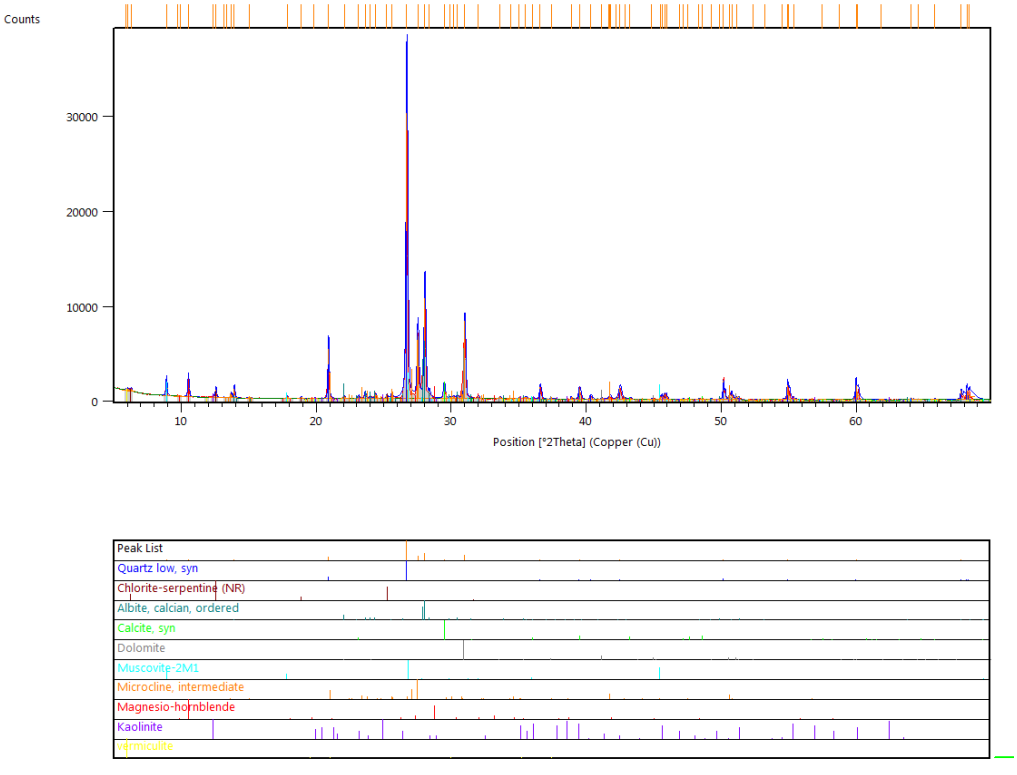

Figure A4. H002-6CS-3 phase ID

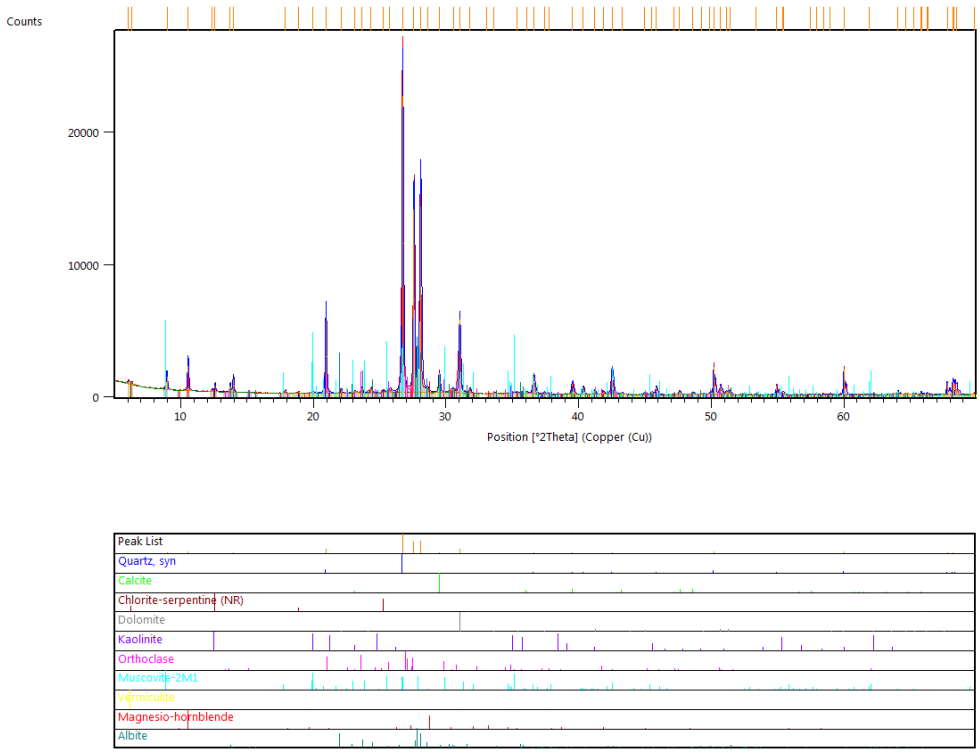

Figure A5. H002-7CS-1 phase ID

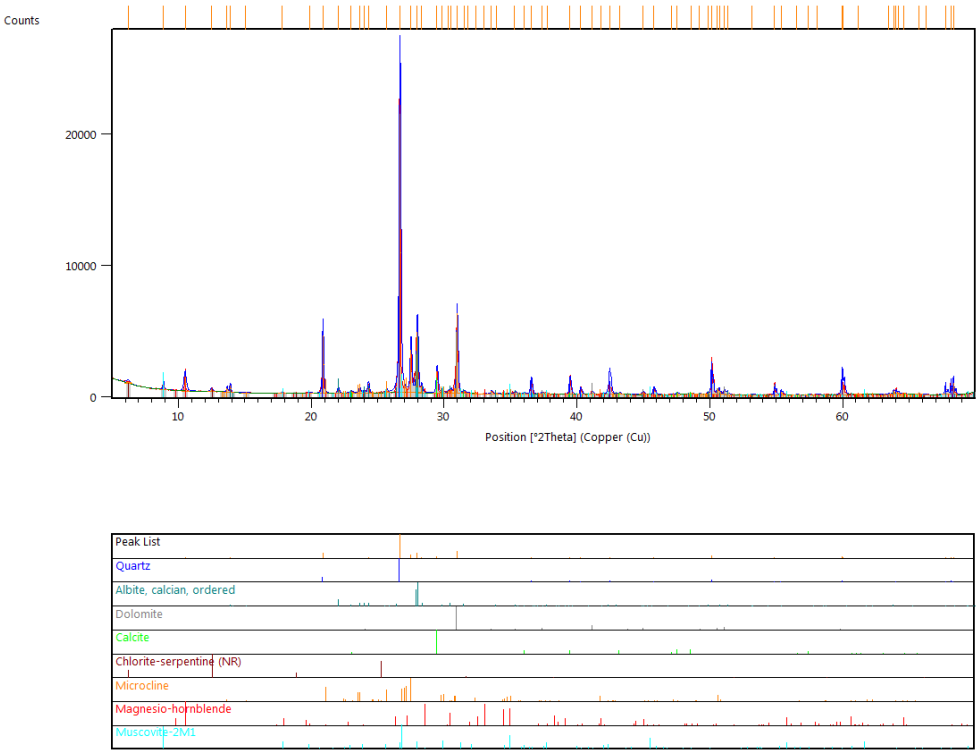

Figure A6. H002-8CS-3 phase ID

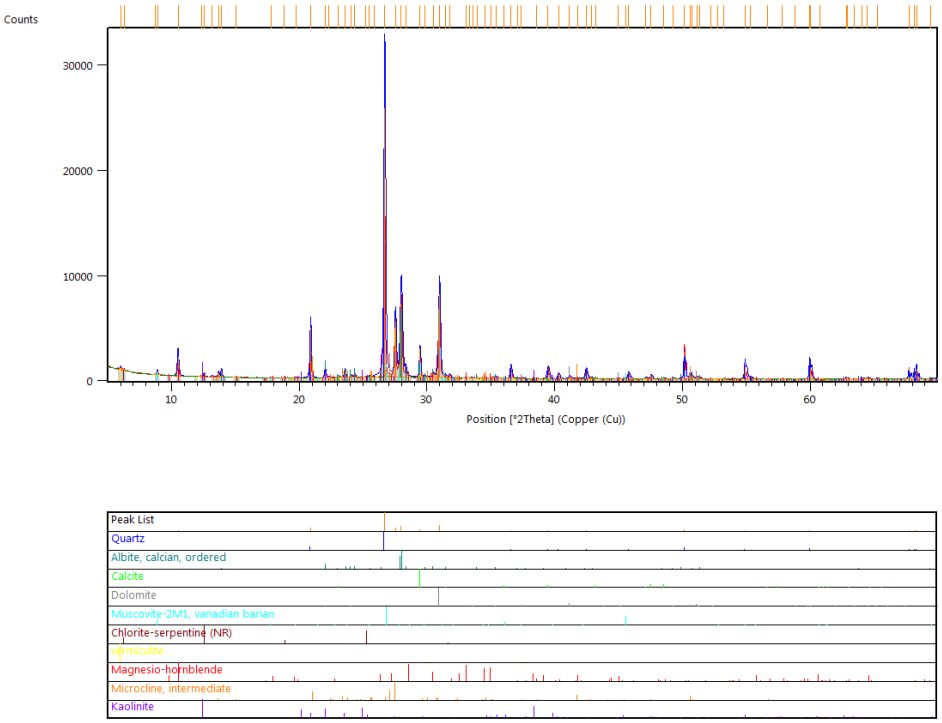

Figure A7. H002-12CS-3 phase ID

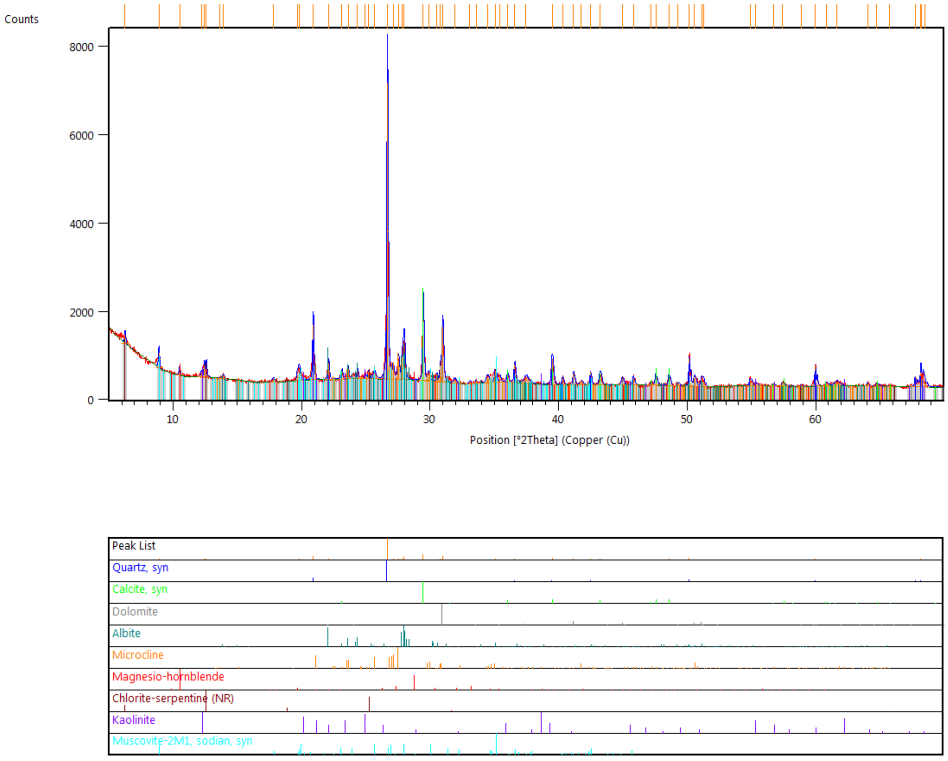

Figure A8. H005-1FB-1 phase ID

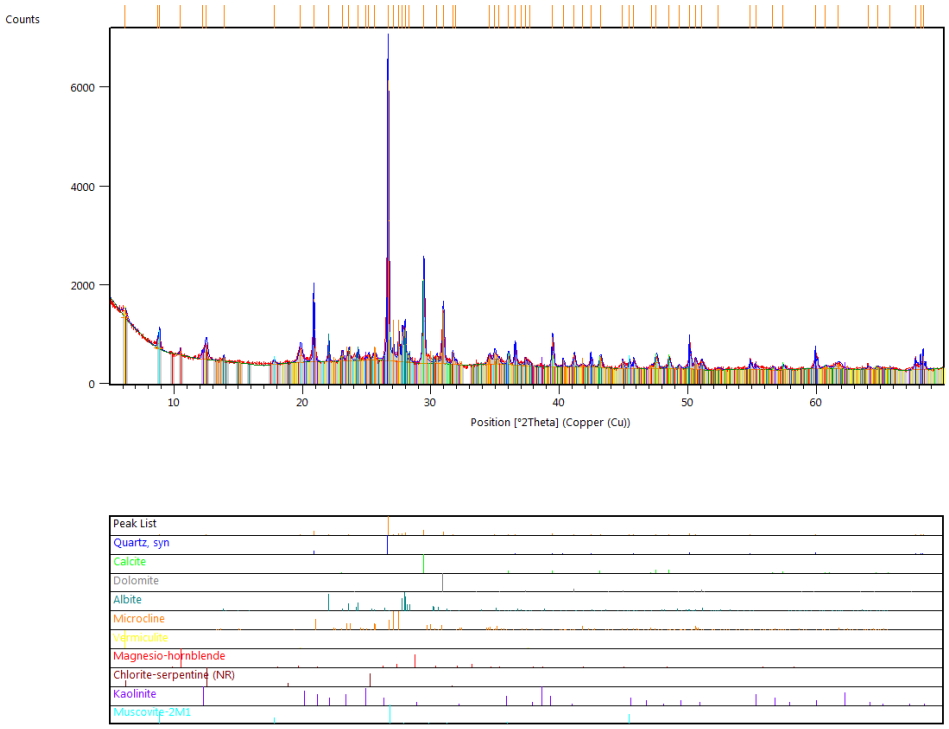

Figure A9. H005-1FB-2 phase ID

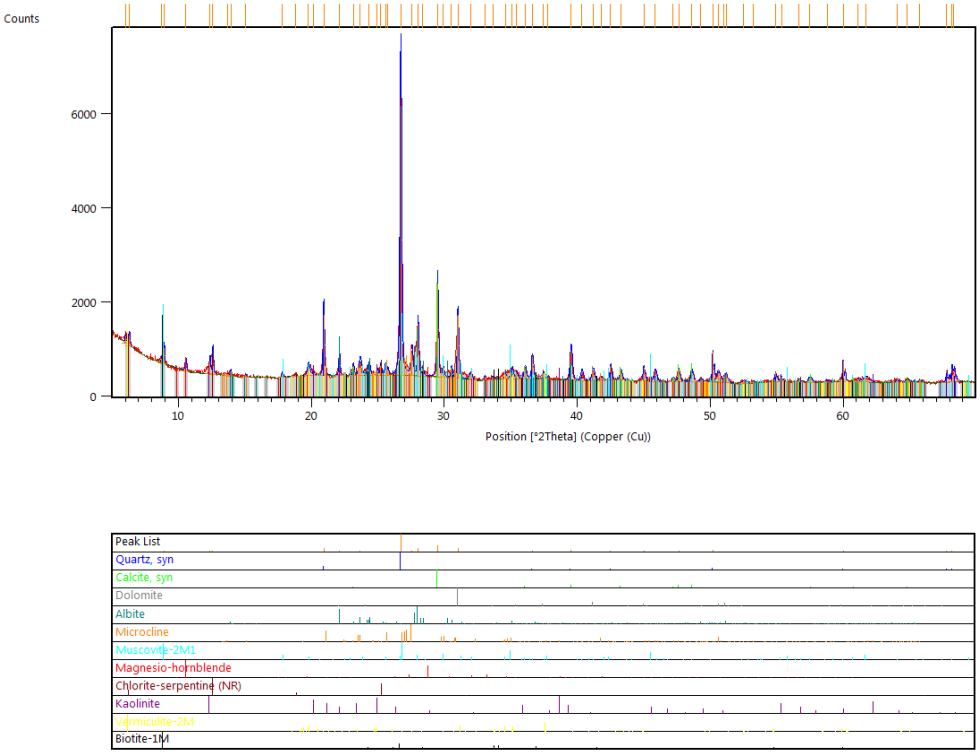

Figure A10. H005-1FB-3 phase ID

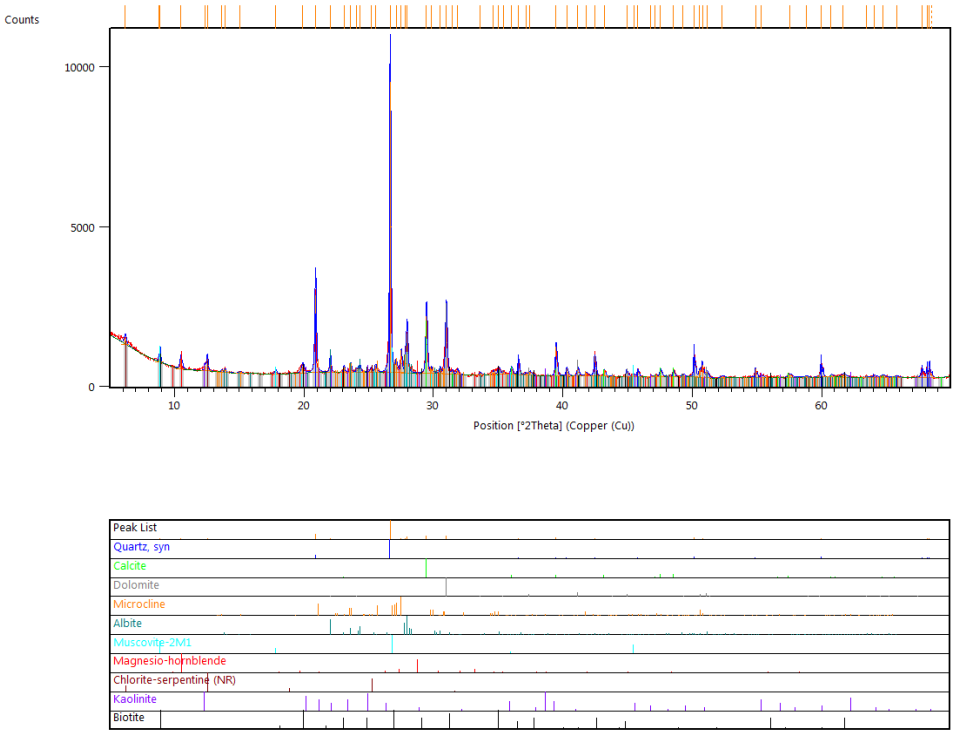

Figure A11. H005-2FB-1 phase ID

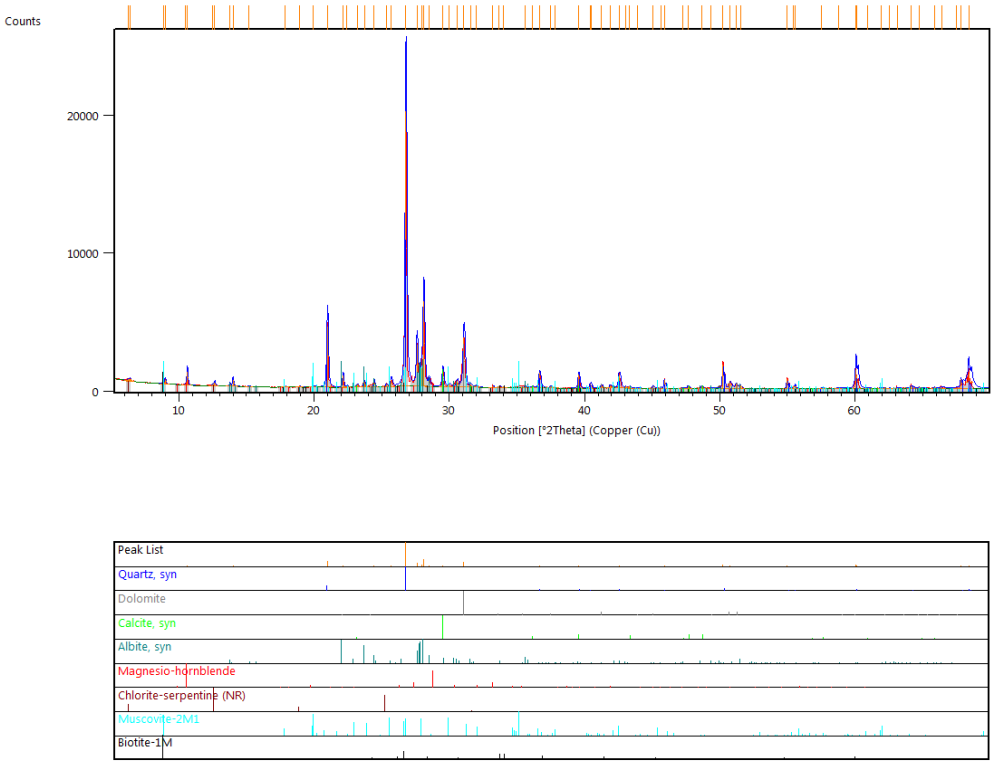

Figure A12. H005-3FB-3 phase ID

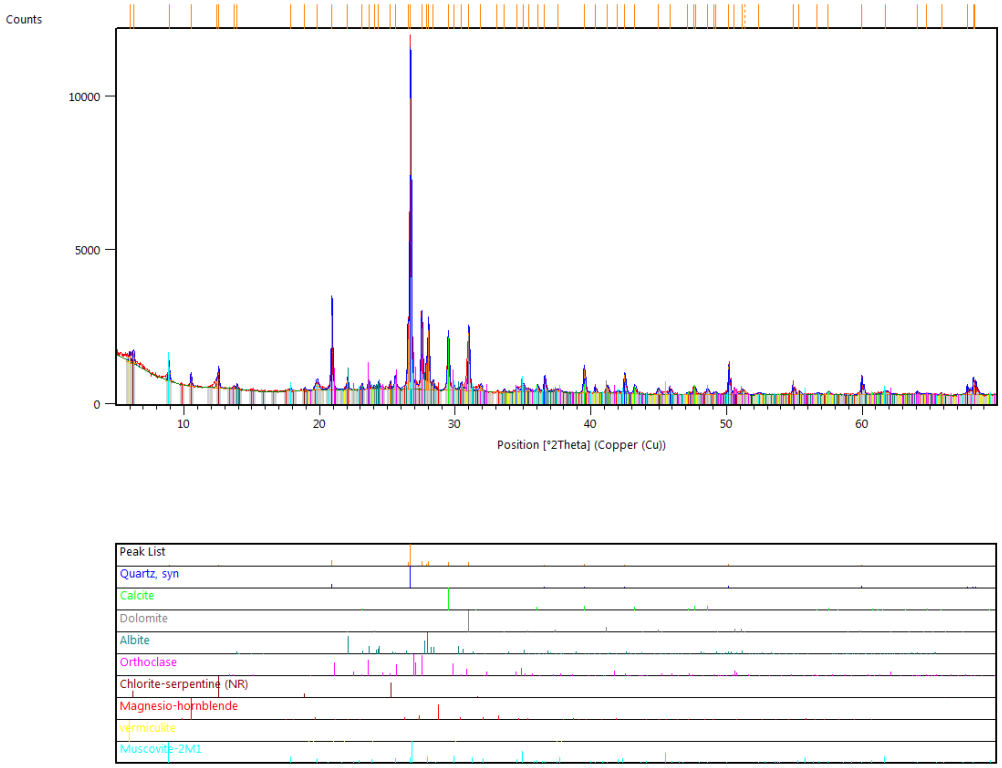

Figure A13. H005-4FB-3 phase ID

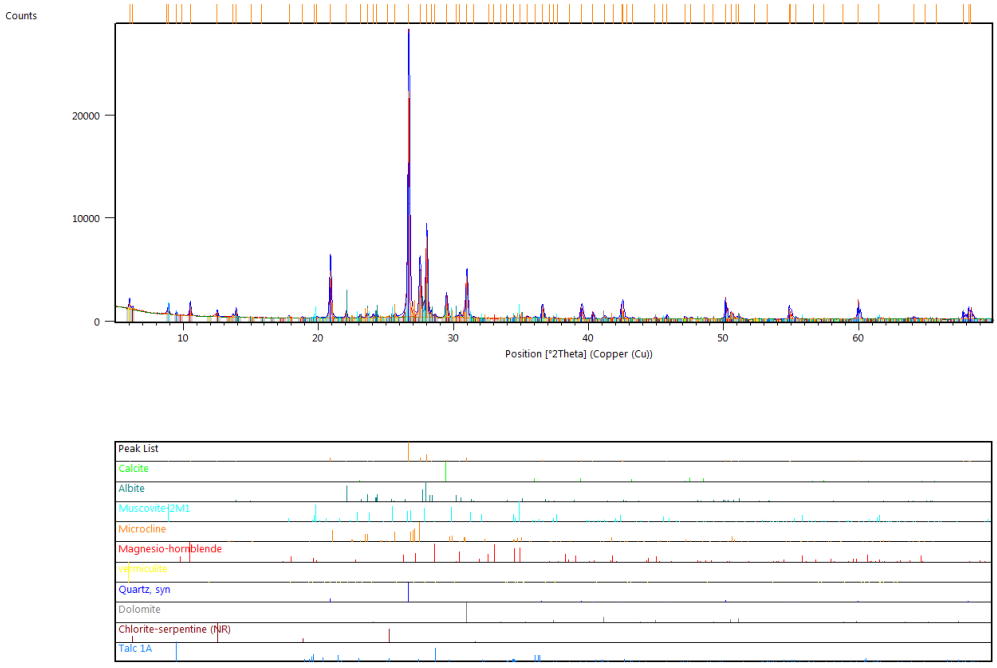

Figure A14. H005-4FB-4 phase ID

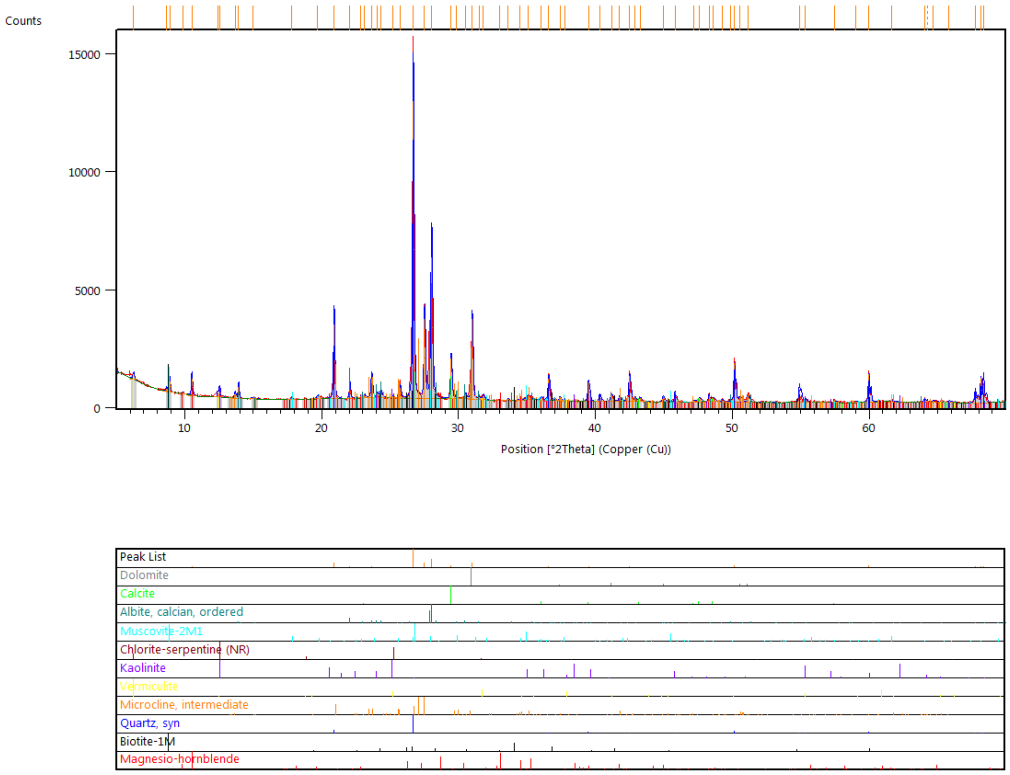

Figure A15. H005-9FB-1 phase ID

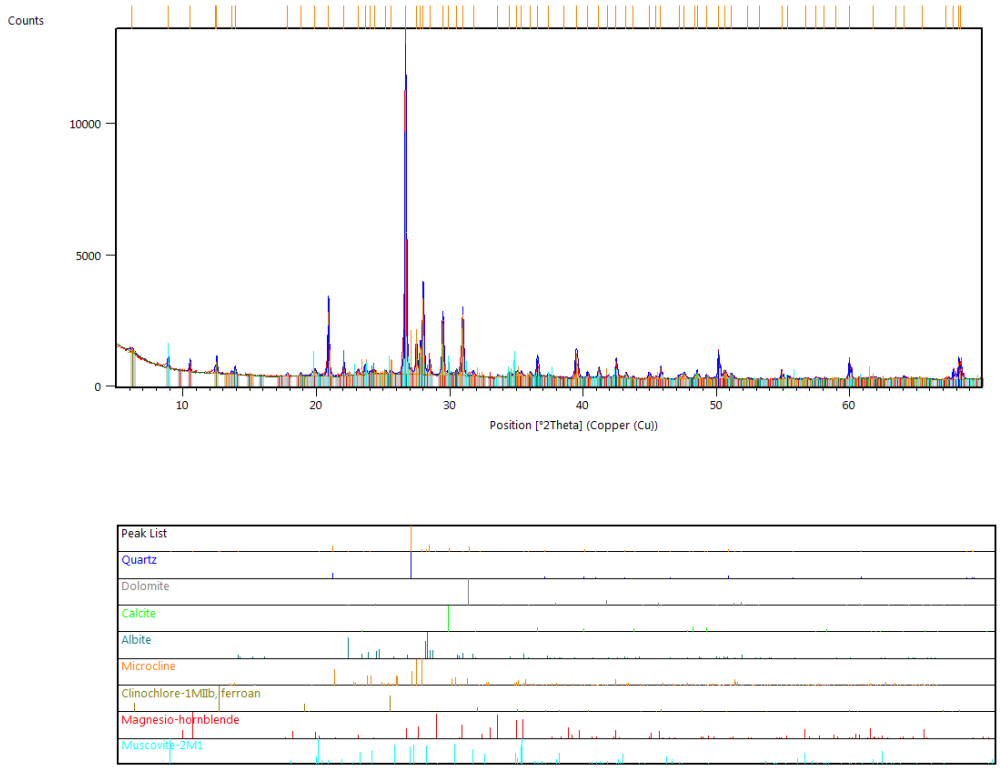

Figure A16. H005-9FB-4 phase ID

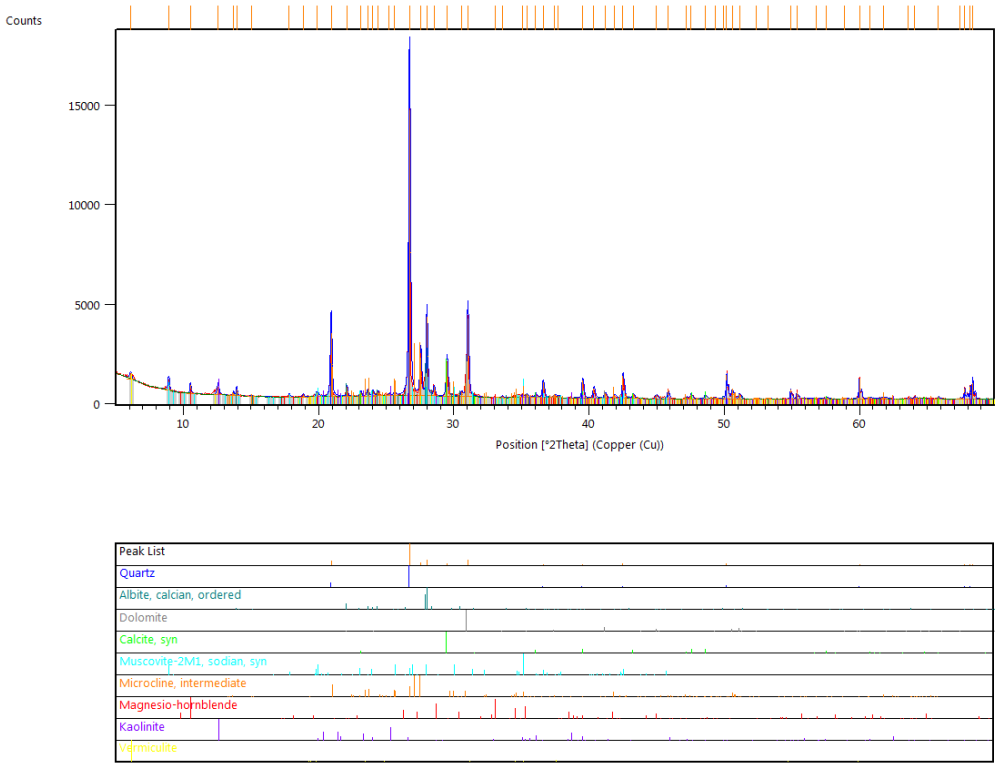

Figure A17. H005-9FB-4 phase ID

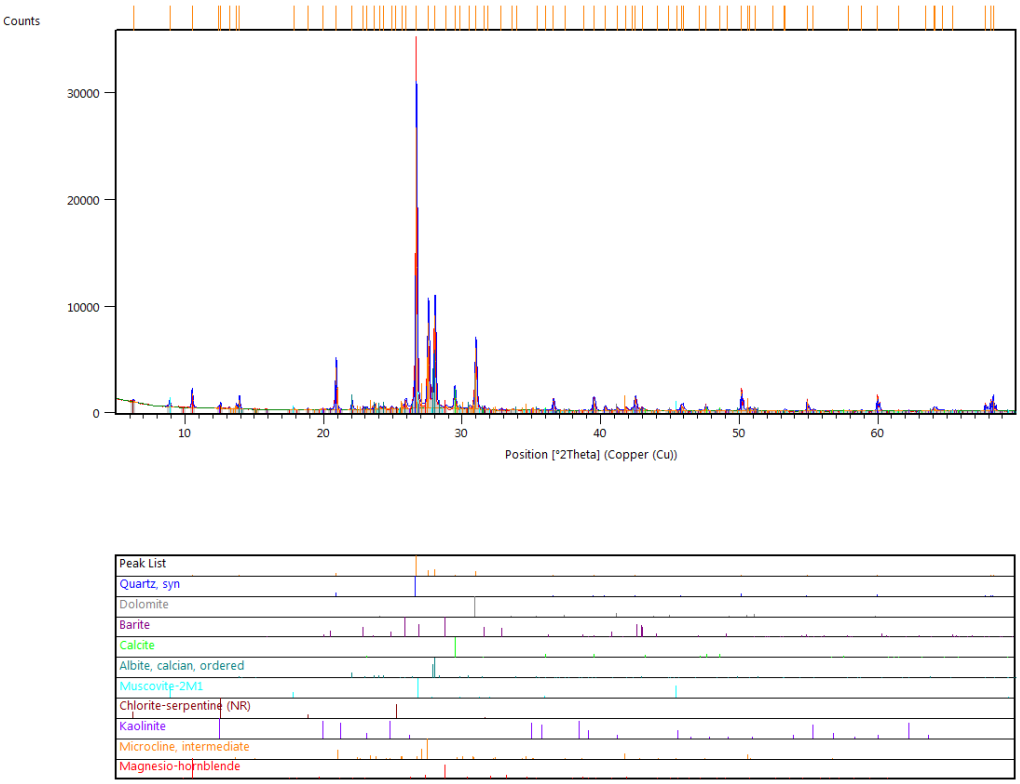

Figure A18. H005-12FB-3 phase ID